# The Effects of Peeling on Finite Element Method -based EEG Source Reconstruction

Santtu Söderholm[a], Joonas Lahtinen[a], Carsten H. Wolters[b,c], Sampsa Pursiainen[a]

[a] *Computing Sciences, Tampere University, Korkeakoulunkatu 3, Tampere, 33014, Pirkanmaa, Finland*
[b] *Institute for Biomagnetism and Biosignalanalysis, University of Münster, Schlossplatz 2, Münster, 48149, Nordrhein-Westfalen, Germany*
[c] *Otto Creutzfeldt Center for Cognitive and Behavioral Neuroscience, University of Münster, Schlossplatz 2, Münster, 48149, Nordrhein-Westfalen, Germany*

**Abstract**

The problem of reconstructing brain activity from electric potential measurements performed on the surface of a human head is not an easy task: not only is the inverse problem fundamentally ill-posed, but the methods utilized in constructing a synthetic forward solution themselves contain many inaccuracies. As an example the usual method of modelling primary currents in the human head via dipoles brings about at least two modelling errors: one from the singularity introduced by the dipole, and one from placing such dipoles near conductivity discontinuities in the active brain layer boundaries.

In this article, we observe how the removal of possible source locations from the vicinity of active layer surfaces affects the localisation accuracy of two inverse methods, Standardized Low-Resolution Tomography (sLORETA) and Dipole Scan, at different signal-to-noise ratios (SNR), when the $H(\mathrm{div})$ source model is used. This source location restriction is achieved by setting a peeling depth or a threshold distance $d_{\mathrm{p}}$, that acceptable source positions must have from active gray matter boundaries. Our aim is to understand the full effect and potential of peeling with a multi-compartment and high-resolution head model, in which the cortical activity is limited into a thin and strongly folded layer of gray matter.

Our results suggest that peeling can significantly improve the overall regularity of the reconstructed distributions, when a suitable peeling depth and a low enough noise level are selected. The applied inverse algorithm and brain compartment under observation also affect the accuracy.

*Keywords:* EEG, finite element method, lead field, source localisation, sLORETA, Dipole Scan, H(div),
*PACS:* 41.20.Cv, 42.30.Wb,
*2000 MSC:* 65N30, 92C55

## 1. Introduction

The electroencephalography (EEG) forward problem of attempting to mathematically construct the electric potentials $u$ produced by given electrical activity $\mathbf{J}_{\mathrm{p}}$ in the human brain is almost a century-old endeavour [1][2], the requirements of which are fairly well known. For simplified cases, such as homogenous and unbounded conductors, layered conductors and spherical head models, there exist semi-analytical or formulaic solutions [3][4][5]. However, realistic head geometries require the application of numerical approaches, such as the finite difference [6], boundary element [7][8], or finite element methods [9][10][11] to solve the same problem.

The primary currents $\mathbf{J}_{\mathrm{p}}$ themselves are often modelled as electrical dipoles in EEG. One of the problems that arises in formulating the forward problem in this way is the appearance of singularities in the potential field $u$ generated by the dipoles [9][10]: $u$ is inversely proportional to the distance $r$ from the dipole position $\mathbf{x}$, where $u$ is singular. This has implications on the convergence of numerical methods, which attempt to build the forward solution based on a finite element model of the human head, with conductivity jumps between the neighboring brain compartments. More specifically, in the finite element formulation [12], the load vector $\mathbf{f}$ is not well-defined in the case of a singular source. The accuracy of the forward solution also ends up being reduced, as a dipole is placed near a boundary of an active compartment [9][12][13].

To tackle the issue of potential singularities themselves, a so called *subtraction method* [9][10][14][15] has been recently utilized. It involves splitting the potential field $u$ into a sum of two separate potentials, a problematic singularity potential $u^{\infty}$ and a correction potential $u_{\mathrm{corr}}$, and solving the EEG forward problem in the case of $u_{\mathrm{corr}}$. This amounts to removing the singularity from the dipole model.

Another approach to handling the dipolar singularity is the so-called $H(\mathrm{div})$ model [12][13], which assumes a higher smoothness or regularity at the primary source level, being neurophysiologically well motivated [7][16]. Assuming such smoothness, the $H(\mathrm{div})$ approach resolves the ill-definedness of the load vector $\mathbf{f}$, by replacing the theoretical dipole with a non-singular function. This is achieved by requiring that the model of a dipole is square-integrable in the finite element domain $\Omega$, or belongs to the space $H(\mathrm{div}) = H(\mathrm{div},\Omega)$, whose elements can be constructed as linear combinations of divergence-conforming basis functions. Here dipolar moments $\mathbf{d}$ are approximated by a vector, whose orientation is defined by a set of finite element nodes surrounding a central node, taking into account the *a priori* information about the

primary currents which are normally oriented to the surface of the gray matter layer. Since the vector is only supported by a few nodes, it is very focal and is therefore able to fit inside the thin gray matter layer, if the resolution of the mesh is fine enough.

Both approaches suffer from inaccuracies near conductivity jumps. In the case of $H(\mathrm{div})$, which is used in this work, a dipole might still be placed at the very edge of an active brain compartment, with some of the supporting finite element nodes in a neighboring compartment. Due to the different conductivities in the different compartments, the volumetric current between the compartments ends up being altered, resulting in a change in the modelled potential field $u$ [13]. For the subtraction method, its numerical accuracy decreases as a dipole is placed near a conductivity jump, as the upper bound of its error is a function of the distance from the conductivity jump [9].

The main purpose of this article is to find out how limiting the possible source positions to a given distance $d_{\mathrm{p}}$ from conductivity jumps affects the localisation accuracy of two inverse methods, *Standardized Low-Resolution Tomography* (sLORETA) [17] and Dipole Scan [18], when a set of synthetic EEG measurements has been given to them as input. This is all performed in an adapted high-resolution finite element mesh, with a base resolution of 2 mm, with additional refinements performed on the active surfaces, to accommodate the $H(\mathrm{div})$ approach in the 1–4 mm-thick gray matter layer [19]. The motivation behind choosing the two inverse methods lies in the fact that sLORETA has been suggested to localise *distributed* patch-like sources in the entire head volume, if the number of sources and the amount of measurement noise remains low, with SNR > 10 dB [20][21]. Dipole Scan has been shown to work well in the case of cortically constrained single-dipole EEG reconstructions, with only a few millimeters' spatial deviations between reconstructions and original source dipoles, in the simulation studies of [22].

In this article, Section 2 will focus on discussing the duality between forward and inverse problems, and how the well-formedness of a forward solution might be tested via the *relative difference measure* (RDM) and *magnitude measure* (MAG). We also explain, how the *peeling*, or removal of possible source positions from surfaces of active brain layers, is performed at the start of the forward algorithm, and how it affects the localisation errors of sLORETA and Dipole Scan, through its influence on the forward solution. In Section 3, we then present our results, evaluate the performance of the peeling algorithm, compare the numerical forward solver to an analytical one via RDM and MAG and, finally, see how the peeling of possible source locations affects the localisation accuracy in a realistic, magnetic-resonance-imaging-based multicompartment head model. In Section 4, results are discussed, Section 5 summarizes our results and Section 6 presents possible future directions of study. Appendix A also presents how Zeffiro Interface [11][12][23][24][25][26], an open software package for multidisciplinary finite-element-based forward and inverse simulation, was used to produce the results in this study.

## 2. Methods and models

### 2.1. Mathematical methods

For the purpose of testing inverse reconstructions of brain activity, we apply the MATLAB-based software suite Zeffiro Interface [11][24], which builds $H(\mathrm{div})$-based lead field matrices $\mathbf{L}$ for different brain imaging modalities, such as electroencephalography (EEG) or magnetoencephalography (MEG) in a volumetric domain $\Omega$, discretized with a finite element mesh [24]. Here a forward solver refers to finding a scalar or vector field, generated by a (synthetic) set of dipole-like sources or the *primary current distribution* $\mathbf{J}_{\mathrm{p}} \in \mathbb{R}^{3N_{\mathrm{J_p}}}$ at Cartesian positions $\mathbf{X} \in \mathbb{R}^{3N_{\mathrm{J_p}}}$ in the domain $\Omega$, where $N_{\mathrm{J_p}}$ is the number of sources. This is done by mapping $\mathbf{J}_{\mathrm{p}}$ to an electric or magnetic set of sensor positions $\mathbf{S} \in \mathbb{R}^{N_{\mathbf{S}}\times 3}$, placed on the surface of $\Omega$, by multiplying $\mathbf{J}_{\mathrm{p}}$ with the lead field $\mathbf{L} \in \mathbb{R}^{N_{\mathbf{S}}\times 3N_{\mathrm{J_p}}}$ [7]. In other words [11][12]:

$$\mathbf{M} = \mathbf{L}\mathbf{J}_{\mathrm{p}} + \mathbf{E}. \tag{2.1}$$

Here $\mathbf{M}$ could consist of electric potentials $\mathbf{u} \in \mathbb{R}^{N_{\mathbf{S}}}$ or magnetic field strenghts $\mathbf{H} \in \mathbb{R}^{N_{\mathbf{S}}\times 3}$ at the sensors $\mathbf{S}$, and $\mathbf{E}$ is the error arising from numerical approximation and measurement noise. Once $\mathbf{L}$ is constructed, it plays a pivotal role in producing the inverted dipoles or primary current distribution $\mathbf{J}_{\mathrm{p}}^{\wedge}$ in a given volume [27][28]. This is illustrated in Figure 2.1.

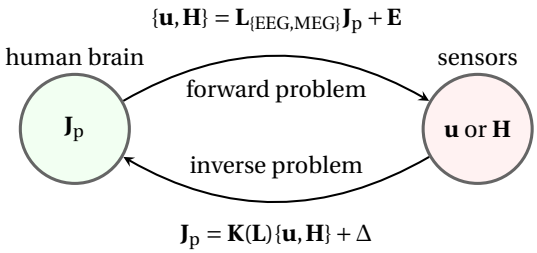


**Figure 2.1:** A simplified [29] illustration of the duality between forward and inverse problems in EEG and MEG imaging. Here $\mathbf{L}$ is the lead field matrix and $\mathbf{K} = \mathbf{K}(\mathbf{L})$ an inversion method -specific kernel, that provides a reconstruction of the original activities $\mathbf{J}_{\mathrm{p}}$ based on the measurements at the sensors. [30]

Regardless of the modality of $\mathbf{L}$ and in the absense of coarse artefacts, the origins of the *localisation error* $\Delta$ of Figure 2.1 in the entire inversion process can be split roughly into 3 components:

$$\Delta = \mathbf{E}_{\mathscr{T}+\mathbf{J}_{\mathrm{p}}} + \mathbf{E}_M + \mathbf{E}_K\,. \tag{2.2}$$

Here $\mathbf{E}_{\mathscr{T}+\mathbf{J}_{\mathrm{p}}}$ is the modelling error resulting from the discretization or tetrahedralization $\mathscr{T}$ of the head model and the configuration such as positioning and orientation of the source space $\mathbf{J}_{\mathrm{p}}$ [31][32][33]. The symbol $\mathbf{E}_M$ represents the error brought to the measurements $\mathbf{u}$ and/or $\mathbf{H}$ by (simulated) measurement noise [34][35][36] and $\mathbf{E}_K$ is an inverse method -specific error brought about by, among other things, the biasing nature of each method, caused by prior assumptions regarding the measurements $\mathbf{M}$ or the primary current distribution $\mathbf{J}_{\mathrm{p}}$ in the derivation of said methods [34][37][38][39].

One of the most significant contributors to the term $\mathbf{E}_{\mathcal{T}+\mathbf{J}_\mathrm{p}}$ in (2.2) is the actual shape and structure of the head model used. It has been reported that using spherical models instead of realistic ones generated by segmenting MRI or CT data increase the localisation error $\Delta$ by as much as 40 mm [40]. On the other hand, inaccuracies in the meshing procedure, such as labeling finite elements into compartments they do not belong to, or not modelling enough different compartments to accurately simulate brain structure also contribute to the error. For example, it has been concluded [41], that the absence of a cerebrospinal fluid (CSF) layer would have detrimental effects on the accuracy of the forward solution $\mathbf{L}$ and the ensuing inverse reconstruction $\mathbf{J}_\mathrm{p}^\wedge$ [42][43][44][45].

The tetrahedralization $\mathcal{T}$ might also affect the generation of the source space $\mathbf{J}_\mathrm{p}$, as it has the possibility of restricting how synthetic sources can be placed into the head model. In the case where $\mathbf{J}_\mathrm{p}$ forms a divergence-conforming field, the source space is directly anchored to the tetrahedra, and interpolated across their faces and edges, due to the presence of a face-intersecting and edgewise divergence-conforming source model [13]. This is visualized in Figure 2.2, where the directions of the dipoles are given by the vectors $\mathbf{d}$. These align with the dipole moments $\mathbf{p}$ of the corresponding dipoles.

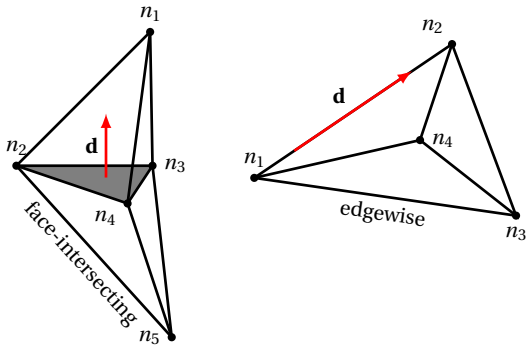


**Figure 2.2:** Face-intersecting and edgewise dipoles. In the first case, the opposing node pair $(n_5, n_1)$ function as the ends of a dipole, whereas in the second case it is the pair $(n_1, n_2)$. The red vectors $\mathbf{d}$ denote the directions of the dipoles from negative to positive end. The $H(\mathrm{div})$ source model places both kinds of sources into the FE mesh. [13]

This holds significance, because as a direct consequence of Maxwell's equations the electric and magnetic components of an electromagnetic field are perpendicular to each other [46]. Hence EEG electrodes are sensitive to the radial dipoles pointing in their direction, whereas MEG sensors best detect tangential sources, that are perpendicular to the ideal EEG orientations [44]. Therefore, both EEG and MEG might fail to detect some source orientations, which are themselves subject to modelling errors.

In this context, the theoretical grounds of the peeling follow from the properties of the local environment of the source position and its relationship to the global solution of the forward problem. The solution can be divided into a local and global component via a Schur complement [47][48], as shown in [13, Appendix A]. The accuracy of the local part will, thereby, affect the accuracy of the global one. Thus, the global accuracy can be improved by enhancing the resolution of the FE mesh in the vicinity of local error sources [48], including the source itself and the discontinuities of the tissue conductivity. The further away the source position is from those discontinuities in relation to the element size, the less there will be global errors magnified due to weak singularities.

The possible causes for the measurement noise component $\mathbf{E}_M$ of the localisation error $\Delta$ are numerous. These include insufficient shielding of the imaging room, poor properties of the measuring equipment, the ill-positioning of the sensors on the scalp, the lack of establishment of proper electrical contact between electrodes and skin via the application of electolyte gel, and so forth. [35][36] To model the uncertainties related to $\mathbf{E}_M$, we add Gaußian noise to the simulated signal. To understand how the added noise affects the reconstruction of $\mathbf{J}_\mathrm{p}$ in the inversion phase, we investigate a sample of inverse estimates obtained with random Gaußian noise realizations.

To finally consider the $\mathbf{E}_K$ component of $\Delta$ in (2.2), the ill-posed nature of the inverse problem needs to be taken into account [38][49][50]. The problem is underdetermined, characterized by a larger number of variables or degrees of freedom than there are equations or other constraints in the forward model. This leads to the need to incorporate *prior-assumptions* regarding the primary current distribution $\mathbf{J}_\mathrm{p}$ of equation (2.1) into the model. This can be achieved by applying *regularization* or *penalty functions* to the related cost function [49][51]. In what follows, we briefly review two inverse methods, sLORETA and Dipole Scan, that represent different approaches to favouring certain kinds of unique estimates $\mathbf{J}_\mathrm{p}^\wedge$ of $\mathbf{J}_\mathrm{p}$.

### 2.2. Inverse methods

In this study, we will utilize two different inverse methods to reconstruct primary source distributions $\mathbf{J}_\mathrm{p}$ in the active compartments of a human brain, based on simulated measurements performed on the scalp: sLORETA [17] or *standardized low-resolution tomography* and Dipole Scan [18]. As described below, both of these methods can be formulated in terms of so-called *spatial filters* $\mathbf{W} = \mathbf{W}(\mathbf{x})$, where following the example of Figure 2.1, the filter matrix $\mathbf{W}(\mathbf{x})$ corresponding to a single source position $\mathbf{x}$ plays the role of the inverse kernel $\mathbf{K}$, biasing the inverse solution in ways indicated by the prior assumptions, related to the inverse method at hand. Once a filter is in place, a reconstruction or its estimator $\mathbf{J}_\mathrm{p}^\wedge$ [52] can be formed as the matrix product [53][54]

$$\mathbf{J}_\mathrm{p}^\wedge(\mathbf{x}) = \mathbf{W}(\mathbf{x})\mathbf{M} \quad \text{or} \quad \mathbf{J}_\mathrm{p}^\wedge(\mathbf{x}) = \mathbf{W}^\mathrm{T}(\mathbf{x})\mathbf{M}, \tag{2.3}$$

where $\mathbf{M}$ is the set of measurements, and using $\mathbf{W}$ versus the transpose $\mathbf{W}^\mathrm{T}$ depends on how $\mathbf{W}$ is formulated.

#### 2.2.1. Standardized Low-Resolution Tomography (sLORETA)

The inverse method sLORETA is a modification of the classic Tikhonov-regularized minimum-norm estimation

method [7][15], with the modification of normalizing the resulting reconstructions $\mathbf{J}_\mathrm{p}^\wedge$ by the square root of the *resolution matrix* [54][55][56]

$$\mathbf{KL} = \mathbf{L}^\mathrm{T}\left(\mathbf{LL}^\mathrm{T} + \lambda\mathbf{I}\right)^{-1}\mathbf{L}. \tag{2.4}$$

Here $\mathbf{I}$ is an identity matrix and $\lambda \geq 0$ is a regularization parameter. The aim of the normalization is to reduce the depth bias, that is completely removed in the case of noiseless data [54].

In the filter matrix formulation, if $(\mathbf{L} \mid \mathbf{x})$ is a restriction of the lead field to its columns corresponding to the single source position $\mathbf{x}$, this is reflected by defining the filter as [54]

$$\mathbf{W}(\mathbf{x}) = \frac{\left(\mathbf{LL}^\mathrm{T} + \lambda\mathbf{I}\right)^{-1}(\mathbf{L} \mid \mathbf{x})}{\sqrt{(\mathbf{L} \mid \mathbf{x})^\mathrm{T}\left(\mathbf{LL}^\mathrm{T} + \lambda\mathbf{I}\right)^{-1}(\mathbf{L} \mid \mathbf{x})}}. \tag{2.5}$$

In our study, the regularization parameter $\lambda$ is chosen according to [57]. A statistical score [52] $\mathbf{J}_\mathrm{p}^\wedge$ indicating the best source position is then formed via the transpose of the filter: $\mathbf{J}_\mathrm{p}^\wedge(\mathbf{x}) = \mathbf{W}^\mathrm{T}(\mathbf{x})\mathbf{M}$.

### *2.2.2. Dipole Scan*

A second inverse method used in estimating source positions in this paper is the so-called *Dipole Scan* method [18], where following the inverse kernel concept of Figure 2.1, a filter matrix $\mathbf{W} = \mathbf{W}(\mathbf{x})$ is first used to give local estimates $\mathbf{J}_\mathrm{p}^\wedge(\mathbf{x})$ of the primary current distribution $\mathbf{J}_\mathrm{p}$ according to (2.3). A Dipole Scan filter $\mathbf{W}$ can be chosen to be the Moore–Penrose pseudoinverse $\mathbf{L}^\dagger = (\mathbf{L}^\mathrm{T}\mathbf{L})^{-1}\mathbf{L}^\mathrm{T}$, which does not perform any kind of filtering on the data [18], or a truncated singular value decomposition (tSVD) of the restriction $(\mathbf{L} \mid \mathbf{x})$ [22][51][58]. The latter of these filters has a regularizing effect on the solution [18][51], meaning the high spatial noise components are not amplified. Hence, it was employed in this study.

With the local estimates in place, Dipole Scan then minimizes the *relative residual variance*

$$\mathrm{RRV}(\mathbf{x}) = \frac{\|\mathbf{M}_\mathrm{avg} - \mathbf{LW}(\mathbf{x})\mathbf{M}_\mathrm{avg}\|^2}{\|\mathbf{M}_\mathrm{avg}\|^2}, \tag{2.6}$$

with $\mathbf{M}_\mathrm{avg}$ being an average measurement, to find a best-fitting reconstruction. Alternatively, Dipole Scan maximizes the complement of RRV, *goodness of fit*

$$\mathrm{GoF}(\mathbf{x}) = 1 - \mathrm{RRV}(\mathbf{x}), \tag{2.7}$$

to determine the best source position.

## *2.3. The lead field algorithm of Zeffiro Interface*

It is known that jump discontinuities in the conductivities of the brain compartments affect the stiffness matrix needed in construction of the finite element forward solution [9][10][13][44]. As (2.2) shows, errors in the forward solution $\mathbf{L}$ also propagate to the inverse solution. Hence the amount of *peeling* of the active brain layers seen in Figure 2.4 **(b)** is also varied slightly, to see how outliers in the reconstruction are affected.

To this end, the lead field routine of Zeffiro Interface was augmented to first peel off the unwanted source positions within the distance of $d_\mathrm{p}$ from the active layer surfaces, and only then start the lead field construction and source positioning. The algorithm now has the following structure:

1. use the peeling algorithm to select a true subset of the active brain elements and evenly distribute allowed source positions into those tetrahedra,
2. build a *stiffness matrix* $\mathbf{A} \in \mathbb{R}^{N_\mathbf{N} \times N_\mathbf{N}}$ [11][59] for the finite element mesh, where $N_\mathbf{N}$ is the number of finite element nodes,
3. use $\mathbf{A}$ to build a *transfer matrix* $\mathbf{T} \in \mathbb{R}^{N_\mathbf{N} \times N_\mathbf{S}}$ [10][13][60][61], which maps measurements from the sensors to finite element nodes and vice versa [15][62], by solving one linear system per sensor position,
4. build a source space interpolation matrix $\mathbf{D} \in \mathbb{R}^{N_\mathbf{N} \times 3N_\mathbf{J_p}}$ based on the $H(\mathrm{div})$ source model [12][13][30], which maps potentials from source positions to the finite element nodes, with either *position-based optimization* (PBO) [63] or *mean position and orientation* (MPO) [30] used as optimization methods,
5. compute the lead field as the matrix product $\mathbf{L} = \mathbf{T}^\mathrm{T}\mathbf{D}$ and
6. subtract the mean measurement from each column of $\mathbf{L}$ to set the zero potential level of the solution.

To further disseminate on how the peeling algorithm `zef_deep_nodes_and_tetra` functions, it

1. determines the surface- and non-surface nodes of the given active layers,
2. finds the nodes that are unacceptably close to the surface nodes, by placing spheres of radius $d_\mathrm{p}$ at each surface node, and checking which mesh nodes are within these spheres and
3. observes which tetra have all 4 of their nodes outside of the surface-node-centric spheres. If this is not true for a tetrahedron, the tetrahedron is disqualified from the set of possible source locations.

Note that step 3 results in the outermost layer being peeled off, regardless of what the peeling depth $d_\mathrm{p}$ is, as each surface node is itself inside of the sphere centered on it. This is desirable, as it removes the chance of singularities due to conductivity discontinuities appearing in the solution. To see how the computations were performed in practise, see Appendix A.

## *2.4. Head models*

To compute the forward and inverse solutions to the biomagnetic source modelling problem presented in the previous subsection, one has to discretize the volume conductor such that a computer can process it. To this end, Zeffiro Interface builds finite element domains from given MRI segmentations [24].

### 2.4.1. *The Ary model and analysis of the forward solution*

Figure 2.3 presents a cross-section of a spherical 3-layer finite element Ary model [4][24] generated in Zeffiro Interface. The spherical volume conductor has a semi-analytic solution to the computation of the lead field $\mathbf{L}$ [4], and hence it provides a useful point of comparison when analysing the goodness of the numerical result.

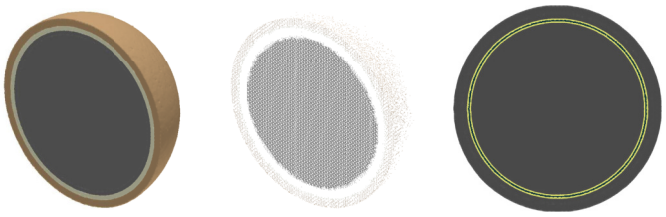

(a) (b) (c)

**Figure 2.3:** Cross sections of a finite element construction of an Ary sphere model. In (**a**), the FE edges are not displayed and the layers in the model are clearly visible. In (**b**), the edges and, therefore, the high resolution of the generated mesh are displayed. Subfigure (**c**) displays the location of the thin gray matter layer, with the yellow streaks indicating its inner and outer boundaries.

Later on, we analyse the differences between the numerical and analytical solutions to the forward EEG problem using the relative difference measure [13][41][64]

$$\mathrm{RDM} = \left\| \frac{\mathbf{L}_\mathrm{n}}{\|\mathbf{L}_\mathrm{n}\|_{2,1}} - \frac{\mathbf{L}_\mathrm{a}}{\|\mathbf{L}_\mathrm{a}\|_{2,1}} \right\|_{2,1} \tag{2.8}$$

and magnitude measure [13][64][65]

$$\mathrm{MAG} = \left| 1 - \frac{\|\mathbf{L}_\mathrm{a}\|_{2,1}}{\|\mathbf{L}_\mathrm{n}\|_{2,1}} \right|. \tag{2.9}$$

Here $\mathbf{L}_\mathrm{a}$ and $\mathbf{L}_\mathrm{n}$ are the semi-analytical [4] and numerical lead fields, and $\|\mathbf{L}\|_{2,1}$ denotes the 2-norm of $\mathbf{L}$ along its rows. The closer the measures are to 0, the better the correspondence.

### 2.4.2. *Realistic head model and localisation error*

In addition to the spherical head model, we also take a look at a finite element discretization of an MRI-based multicompartment human head model [66] seen in Figure 2.4. Whereas the Ary model was used to analyse the performance of our forward solver, described in Section 2.3, the purpose of the realistic model was to function as the domain of our inverse computations.

To evaluate the localisation error $\Delta$ of equation (2.2), 10 000 synthetic sources were placed evenly into the active regions of the volume conductor: *Cerebellum cortex*, *Amygdala*, *Thalamus*, *Caudate*, *Nucleus accumbens*, *Putamen*, *Hippocampus*, *Pallidum*, *Brain stem* and *Ventral Diencephalon*. Then a lead field $\mathbf{L}$ corresponding to these sources was computed, as specified in subsection 2.3. For each source given by the position–direction–amplitude triplet $(\mathbf{x}, \mathbf{d}, a)$, synthetic measurements $\mathbf{M}_{(\mathbf{x},\mathbf{d},a)}$ were constructed according to

$$\mathbf{M}_{(\mathbf{x},\mathbf{d},a)} = a\,(\mathbf{L} \mid \mathbf{x})\,\mathbf{d} + 10^{-\mathrm{SNR}/20}\mathbf{n}, \tag{2.10}$$

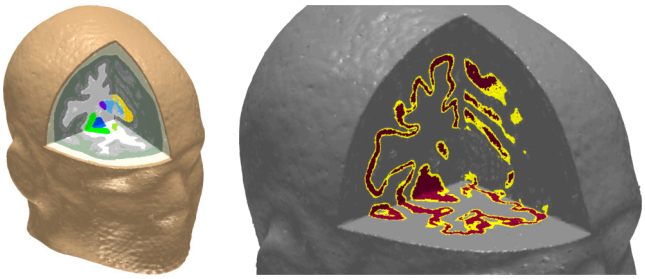

(a) (b)

**Figure 2.4:** A realistic head model used in the computations with Zeffiro Interface. (**a**) shows a cross section of the head with different brain compartments visible, whereas (**b**) shows the active layers in dark red and yellow, with the yellow streaks indicating peeled off tetrahedra. The peeling depth used was 0.1 mm. The active brain compartments include *Cerebellum cortex*, *Amygdala*, *Thalamus*, *Caudate*, *Nucleus accumbens*, *Putamen*, *Hippocampus*, *Pallidum*, *Brain stem* and *Ventral Diencephalon*.

with $\|\mathbf{d}\| = 1$, $a > 0$, and the notation $(\mathbf{L} \mid \mathbf{x})$ indicating a restriction of $\mathbf{L}$ to the columns corresponding to the dipole position $\mathbf{x}$. Here SNR is the noise level in decibels, as in [SNR] = dB, and $\mathbf{n}$ is a normally distributed random variable, with mean $\mu = 0$ and variance $\sigma^2 = 1$.

With the simulated measurements $\mathbf{M}_{(\mathbf{x},\mathbf{d},a)}$ in place, they were then inverted with sLORETA and Dipole Scan, to produce a set of estimates $\{\mathbf{d}_k^\wedge\}$: one $\mathbf{d}_i^\wedge$ for each $\mathbf{x}_i$ in the original source space[1]. The position $\mathbf{x}_I$ of the most focal reconstruction was sought by finding the index $I$ of the direction $\mathbf{d}_i^\wedge$ with the largest norm or dipole moment, as in

$$I = \operatorname{ind}\max_i \|\mathbf{d}_i^\wedge\|_2\,, \tag{2.11}$$

following the *maximum principle of source localization* [13][67][68]. The localisation error $\Delta$ was then evaluated as the root-mean-square of the Cartesian components:

$$\Delta(\mathbf{x}_i) = \frac{1}{\sqrt{3}}\|\mathbf{x}_i - \mathbf{x}_I\|_2\,. \tag{2.12}$$

To measure the width of a reconstruction peak related to a source position $\mathbf{x}_i$ we also use the so-called *spatial dispersion* measure [69]

$$\mathrm{SD}(\mathbf{x}_i) = \sqrt{\frac{\sum_k (d_{k,i}\|\mathbf{p}_k\|)^2}{\sum_k \|\mathbf{p}_k\|^2}}\,, \tag{2.13}$$

where $k$ ranges over the indices of the source positions $\mathbf{x}_k$ in a given ROI around $\mathbf{x}_i$, $\mathbf{p}_k$ are the dipole moments of the reconstructions in the ROI, and $d_{k,i}$ is the distance of the $k$th dipole in the ROI from $\mathbf{x}_i$. In this study, it is observed how varying the peeling depth $d_\mathrm{p}$ affects the measure (2.13).

## 3. Results

### 3.1. *Evaluating the peeling algorithm*

We start off with a discussion on how well the peeling algorithm itself works. Figure 3.1 presents the effects of refining the gray matter layer of the Ary model of Figure 2.3 on its

[1] Constituting an inverse crime. [51]

*peeling*, the disqualification of nodes and associated tetrahedra from the set of valid source positions. The peeling was performed within the distances of 0.5 and 1.0 mm from the inner and outer surfaces of the thin gray matter layer. We consider peeling to be necessary, because placing $H(\mathrm{div})$ dipoles in positions of conductivity discontinuities would cause significant forward errors [13].

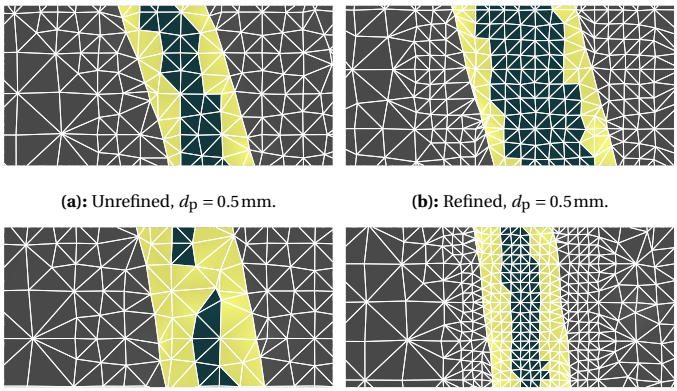

**(a):** Unrefined, $d_\mathrm{p} = 0.5\,\mathrm{mm}$. **(b):** Refined, $d_\mathrm{p} = 0.5\,\mathrm{mm}$.

**(c):** Unrefined, $d_\mathrm{p} = 1.0\,\mathrm{mm}$. **(d):** Refined, $d_\mathrm{p} = 1.0\,\mathrm{mm}$.

**Figure 3.1:** The effects of mesh refinement on *peeling*, or the disqualification of tetrahedra from the set of valid source positions. The yellow triangles indicate which tetrahedra were peeled off the inner and outer surfaces of the thin gray matter layer, after the peeling algorithm had been applied to the mesh. In **(a)** and **(b)** the peeling depth $d_\mathrm{p}$ has been set at 0.5 mm whereas in **(c)** and **(d)** we have $d_\mathrm{p} = 1.0\,\mathrm{mm}$. A more refined mesh produces a more consistent peeling outcome.

As can be observed, refinement plays an important role in the peeling process: it prevents an excessive reduction of possible source positions from the active layer. This can be observed in the unrefined 1.0 mm case shown in Subfigure **(c)**, where a hole is punched through the gray matter layer. This means that a perfectly valid dipolar source location is excluded from the possible set of source positions during forward modelling, or the computation of the lead field matrix $\mathbf{L}$. Taking a closer look at the realistic head model of Figure 2.4 **(b)** also displays a similar effect with a peeling depth of 0.1 mm, which is displayed in Figure 3.2.

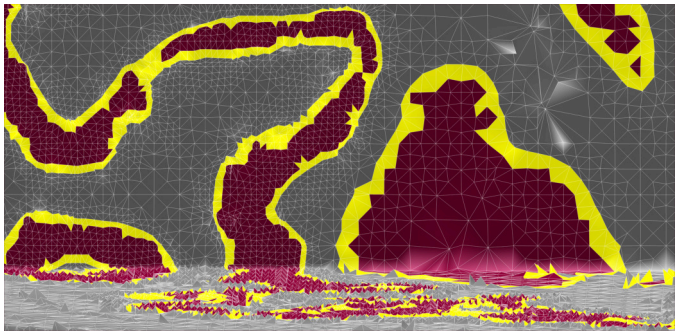

**Figure 3.2:** A portion of the 4 mm thick active layers (dark red + yellow) of Figure 2.4 **(b)**, displayed with the edges of the finite element mesh visualized, but with only 0.1 mm peeling (yellow).

Peeling will remove all those tetrahedra with one or more nodes closer than a given peeling depth to the surface. The reason for this is to make sure that at least one layer of tetrahedra is removed, to avoid source placement in tetrahedra, that are right next to another compartment with possibly differing conductivity.

It turns out that even with the refinement performed on the surface of the active gray matter layer, there are still parts of the compartment which are not fine enough with 0.1 mm peeling, and hence holes in possible source positions, such as the ones seen in the upper left and right corners of Figure 3.2, are formed. This is again due to the requirement that at least one tetrahedral surface layer is removed from the set of possible source positions, which results in the effective peeling depth being greater than the low numerical value provided by the user. The peeling algorithm then seems to function as intended.

### 3.2. *Measuring the goodness of the forward solver against an analytical model*

Figure 3.3 contains box plots [70] of the measures RDM of equation (2.8) and MAG of equation (2.9), when PBO described in Section 2.3 was used for source interpolation, in the case of the analytical model of Figure 2.3. The base resolution of the mesh was 2 mm, with refinement referring to the surface of the active layer being refined as seen in Figure 3.1. *Eccentricity* refers to the relative radius of the position at which the comparison was performed. As suggested by [10], eccentricities of over 98 % are of special interest, as they correspond to where a primary dipole might be physiologically located, somewhere between the external granular and pyramidal layers (layers 2–3) of the cerebral cortex, and hence observed here.

The closer RDM and MAG are to 0, the better the correspondence between the semi-analytical and numerical solutions $\mathbf{L}_\mathrm{a}$ and $\mathbf{L}_\mathrm{n}$. With RDM, in almost all cases the PBO medians remain below the 0.02 limit, except at the highest two eccentricities. The upper outlier quantiles $q_\mathrm{u} = q_{75\%} + 1.5(q_{75\%} - q_{25\%})$, which the whiskers of Figure 3.3 correspond to, mostly remain close to 0.1, with the case of unrefined $d_\mathrm{p} = 0.5\,\mathrm{mm}$ approaching 0.02 at the two highest eccentricities. With MAG, the median remains below 0.04, with the upper quantile $q_\mathrm{u}$ behaving similarly to what was observed with RDM.

Increasing the resolution of the finite element mesh near active layer boundaries via mesh refinement seems to be mostly reducing RDM, especially towards the higher eccentricities. For MAG, the refinement actually seems to increase the median differences between the analytical and numerical lead fields by roughly 0.02, which is seen in the horizontal middle lines of the box plots of Figure 3.3. However, the quantiles $q_\mathrm{u}$ were lowered by a few percent with $d_\mathrm{p} = 0.5\,\mathrm{mm}$, suggesting that refinement has a net positive statistical impact on the result. All in all, the correspondence between $\mathbf{L}_\mathrm{a}$ and $\mathbf{L}_\mathrm{n}$ seems to be appropriate.

### 3.3. *Source localisation in a realistic head model*

In the spirit of Cuffin et al. [71], Tables 3.1–3.2 present mean values $\mu$ of localisation errors $\Delta$ and their standard deviations

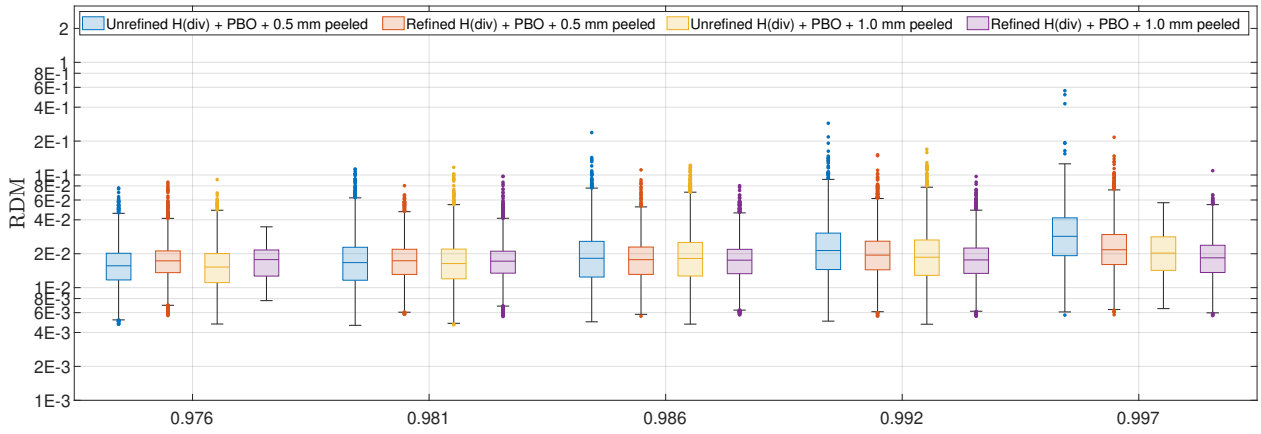


**(a)**

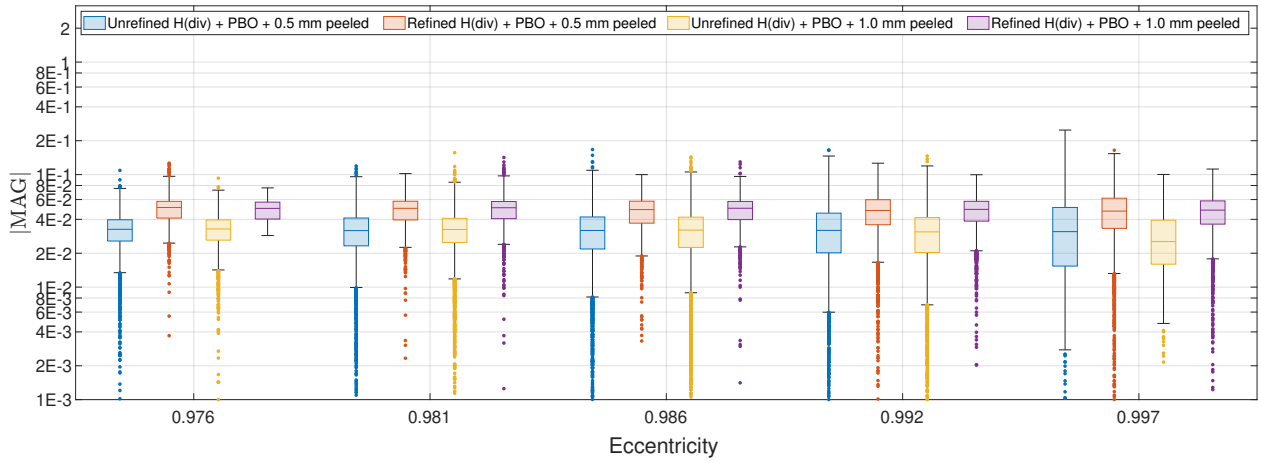


**(b)**

**Figure 3.3:** High-eccentricity (2.8) **(a)** and (2.9) **(b)** for PBO in the case of a spherical Ary model.

$\sigma$ for 10000-source lead fields $\mathbf{L}$, corresponding to different peeling depths $d_p$. The lead fields were inverted 20 times with sLORETA [17] and Dipole Scan [18] at different measurement noise levels, each inversion evaluated with a different white noise realization. The cells of the Tables 3.1–3.2 are color mapped based on the largest $\Delta$ and $\sigma$ in each table.

**Table 3.1:** sLORETA average localisation error $\Delta$ statistics. Here $d_p$ is the peeling depth, $\mu$ is the sample mean and $\sigma$ is the sample standard deviation.

| $d_p$ (mm) | 0.0 | | 0.5 | | 1.0 | |
|---|---|---|---|---|---|---|
| SNR (dB) | $\mu$ (mm) | $\sigma$ (mm) | $\mu$ (mm) | $\sigma$ (mm) | $\mu$ (mm) | $\sigma$ (mm) |
| 5 | 41.76 | 18.88 | 41.57 | 18.90 | 41.57 | 18.72 |
| 10 | 30.84 | 15.62 | 30.62 | 15.55 | 30.77 | 15.43 |
| 15 | 20.45 | 9.57 | 20.35 | 9.52 | 20.66 | 9.54 |
| 20 | 13.81 | 5.69 | 13.73 | 5.71 | 14.01 | 5.80 |
| 25 | 10.76 | 3.36 | 10.70 | 3.36 | 10.78 | 3.46 |
| 30 | 9.87 | 2.04 | 9.81 | 2.05 | 9.79 | 2.12 |

Here Dipole Scan produces superior localisation results when compared to sLORETA, with both low and high SNR levels, which is an expected result in search of a single source, matching the prior model of Dipole Scan. Especially in the case of Dipole Scan, the mean error $\Delta \approx 10.5$ mm reported by Cuffin is reached already at SNR = 15 dB, whereas with sLORETA a value as high as 30 dB has to be used, for comparable values to manifest themselves.

**Table 3.2:** Dipole Scan average localisation error $\Delta$ statistics. The meaning of notations is the same as in Table 3.1.

| $d_p$ (mm) | 0.0 | | 0.5 | | 1.0 | |
|---|---|---|---|---|---|---|
| SNR (dB) | $\mu$ (mm) | $\sigma$ (mm) | $\mu$ (mm) | $\sigma$ (mm) | $\mu$ (mm) | $\sigma$ (mm) |
| 5 | 26.87 | 13.57 | 26.83 | 13.60 | 26.88 | 13.53 |
| 10 | 16.01 | 7.92 | 15.97 | 7.92 | 16.08 | 7.99 |
| 15 | 9.13 | 4.66 | 9.11 | 4.66 | 9.17 | 4.75 |
| 20 | 5.09 | 3.01 | 5.07 | 3.01 | 5.07 | 3.05 |
| 25 | 2.65 | 2.01 | 2.64 | 2.01 | 2.64 | 2.00 |
| 30 | 1.18 | 1.22 | 1.18 | 1.22 | 1.20 | 1.21 |

To graphically observe how the peeling affects outliers of $\Delta$, Figures 3.4 and 3.5 were formed. They display box plots of $\Delta$ against the two lowest noise levels in the case of sLORETA and Dipole Scan, respectively.

In the case of sLORETA, going from a peeling depth of 0 mm to 0.5 mm results in a disappearance of at least few out-

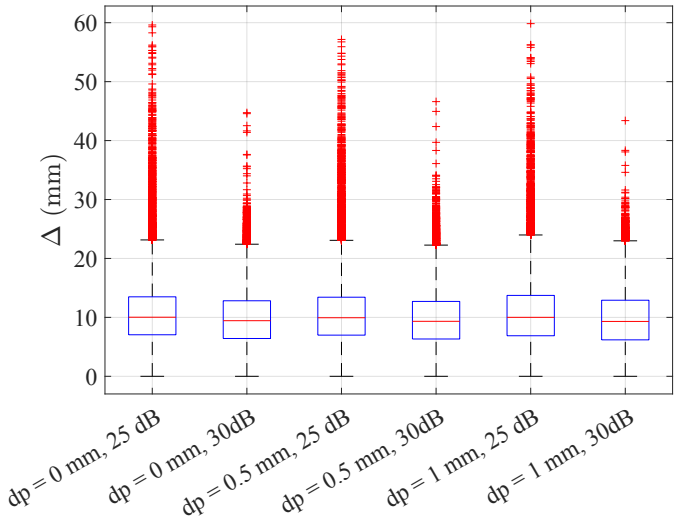


**Figure 3.4:** sLORETA localisation errors Δ against two lowest noise levels and all peeling depths $d_p$.

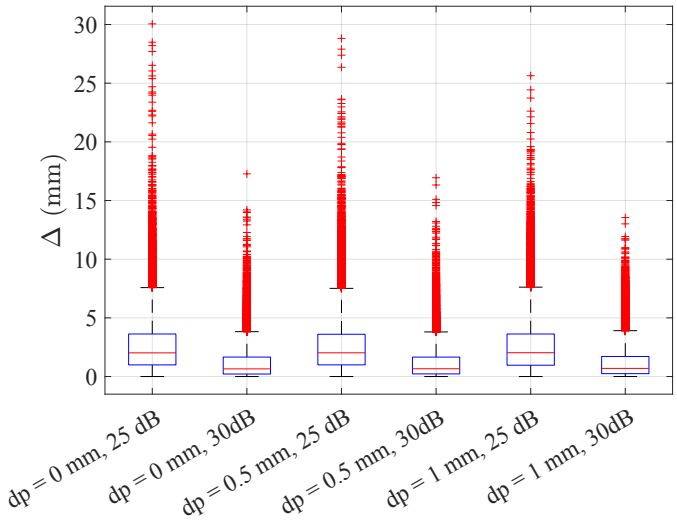


**Figure 3.5:** Dipole Scan localisation errors Δ against two lowest noise levels and all peeling depths $d_p$.

lier markers. Further, moving from 0.5 mm to 1.0 mm peeling depth further reduces the outliers, which is seen in the sparsity of the outlier point clouds. With Dipole Scan, the peeling results are similar, as the extent of outliers is reduced with increased peeling.

To further observe how peeling affects the outliers, Tables 3.3 and 3.4 show the per-noise-level numbers of sources, whose localisation errors satisfy $\Delta > \mu + 2\sigma$, for a sample of 20 reconstructions obtained with a given noise level. Here $\mu$ and $\sigma$ are the expected sample mean and standard deviation values of Δ, provided by Cuffin et al [71, Table 1]. These are contrasted against the numbers of columns in each respective 10000-source lead field **L** by color-mapping each data point against the largest number of columns. Each Cartesian source has coordinates pointing in the $x$-, $y$- and $z$-directions, and hence the number of columns in **L** is threefold, when compared to the mentioned number of sources.

**Table 3.3:** The number of outliers with $\Delta > \mu+2\sigma$, for a sample of 20 sLORETA reconstructions. The expected means $\mu$ and standard deviations $\sigma$ for each noise level have been gathered from [71, Table 1]. Again, $d_p$ refers to the peeling depth.

| $d_p$ (mm) | | | 0.0 | 0.5 | 1.0 |
|---|---|---|---|---|---|
| Number of columns in **L** | | | 30288 | 30459 | 29367 |
| SNR (dB) | $\mu$ (mm) | $\sigma$ (mm) | Number of outliers | | |
| 5 | 10.3 | 5.3 | 29535 | 29710 | 28646 |
| 10 | 10.4 | 5.4 | 21029 | 20965 | 20154 |
| 15 | 10.3 | 4.6 | 12079 | 12104 | 12050 |
| 20 | 10.6 | 4.1 | 5507 | 5552 | 5936 |
| 25 | 10.2 | 3.7 | 3039 | 3120 | 3355 |
| 30 | 9.8 | 3.6 | 2494 | 2582 | 2652 |

**Table 3.4:** The number of outliers with $\Delta > \mu + 2\sigma$, for a sample of 20 Dipole Scan reconstructions. The definitions of $\mu$, $\sigma$ and $d_p$ are the same as in Table 3.3.

| $d_p$ (mm) | | | 0.0 | 0.5 | 1.0 |
|---|---|---|---|---|---|
| Number of columns in **L** | | | 30288 | 30459 | 29367 |
| SNR (dB) | $\mu$ (mm) | $\sigma$ (mm) | Number of outliers | | |
| 5 | 10.3 | 5.3 | 19546 | 19652 | 18923 |
| 10 | 10.4 | 5.4 | 6935 | 6975 | 6866 |
| 15 | 10.3 | 4.6 | 1893 | 1857 | 1836 |
| 20 | 10.6 | 4.1 | 429 | 411 | 411 |
| 25 | 10.2 | 3.7 | 36 | 31 | 24 |
| 30 | 9.8 | 3.6 | 1 | 0 | 0 |

For sLORETA we observed that the more tetra are peeled, the more outliers occur at noise levels below 15 dB. On the other hand, Dipole Scan displays a rather consistent outcome at and below 15 dB noise level, with increased peeling reducing the numbers of outliers. In either case, it seems that noise might be the major contributing factor below the 15 dB mark, with Dipole Scan being slightly more resistant to noise effects.

To get a sense of where the statistical outliers are located, Figures 3.6 and 3.7 display the localisation error Δ of sLORETA and Dipole Scan as a function of position, in the active gray matter compartment. Colors in the figures have been adjusted, such that the obvious outlier positions with $\Delta \geq \mu + 2\sigma$ are highlighted in red. The displayed noise levels are the ones where peeling was discovered to have an observable reduction in Δ.

To illustrate how the localisation error fluctuates locally at lower noise levels, both deep in the brain and more superficially, Figures 3.9 and 3.11 display thalamically focused views of the above images, whereas Figures 3.8 and 3.10 do the same for the cortex. The displayed noise levels are chosen to be the ones, where visible improvements can be seen.

These mappings demonstrate that peeling can help in reducing localisation error universally in the active domain, when the noise level is low enough: for example at 30 dB SNR in Figure 3.11, the localisation error in the part of the frontal

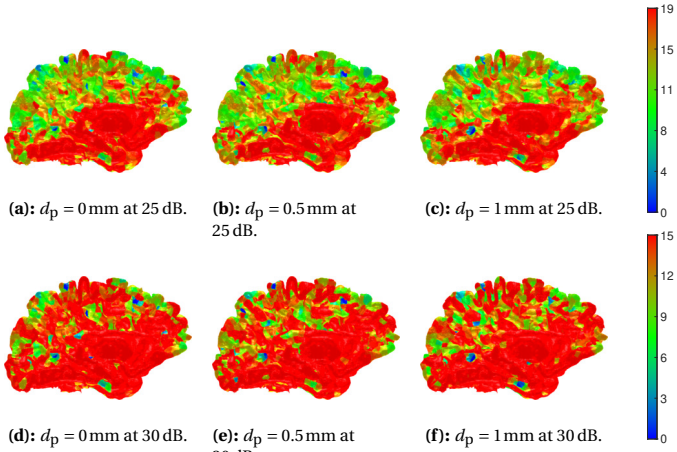


**(a):** $d_p = 0$ mm at 25 dB. **(b):** $d_p = 0.5$ mm at 25 dB. **(c):** $d_p = 1$ mm at 25 dB.

**(d):** $d_p = 0$ mm at 30 dB. **(e):** $d_p = 0.5$ mm at 30 dB. **(f):** $d_p = 1$ mm at 30 dB.

**Figure 3.6:** Sagittal views of localisation error $\Delta = \Delta(\mathbf{x})$ (mm) in the active gray matter layer in the case of sLORETA, contrasted against the different peeling depths $d_p$ of Table 3.1. The red color indicates where $\Delta \geq \mu + 2\sigma$, as in outliers in the entire distribution.

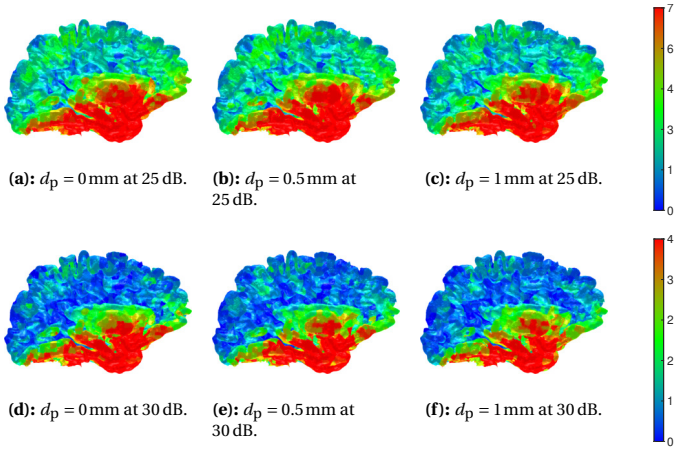


**(a):** $d_p = 0$ mm at 25 dB. **(b):** $d_p = 0.5$ mm at 25 dB. **(c):** $d_p = 1$ mm at 25 dB.

**(d):** $d_p = 0$ mm at 30 dB. **(e):** $d_p = 0.5$ mm at 30 dB. **(f):** $d_p = 1$ mm at 30 dB.

**Figure 3.7:** Sagittal views of localisation error $\Delta = \Delta(\mathbf{x})$ (mm) in the active gray matter layer in the case of Dipole Scan, contrasted against the different peeling depths $d_p$ of Table 3.2. The meaning of the colors is the same as in Figure 3.6.

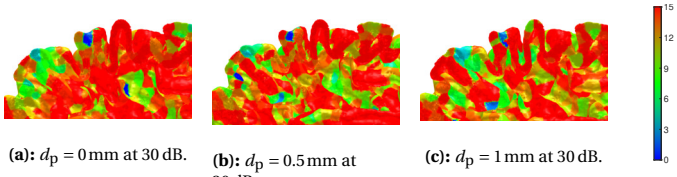


**(a):** $d_p = 0$ mm at 30 dB. **(b):** $d_p = 0.5$ mm at 30 dB. **(c):** $d_p = 1$ mm at 30 dB.

**Figure 3.8:** Focused views of $\Delta = \Delta(\mathbf{x})$ in the parietal region, in the case of sLORETA.

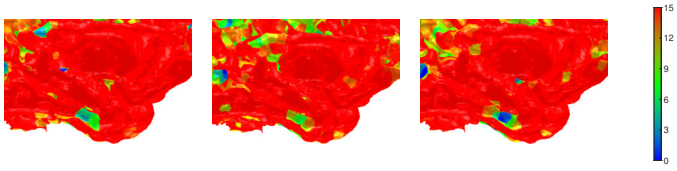


**(a):** $d_p = 0$ mm at 30 dB. **(b):** $d_p = 0.5$ mm at 30 dB. **(c):** $d_p = 1$ mm at 30 dB.

**Figure 3.9:** Focused views of $\Delta = \Delta(\mathbf{x})$ in the thalamic region, in the case of sLORETA.

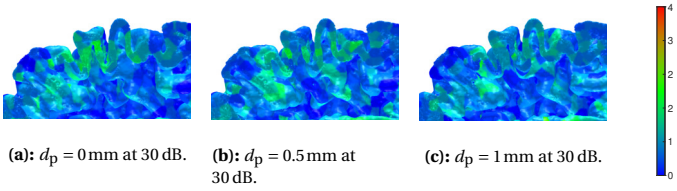


**(a):** $d_p = 0$ mm at 30 dB. **(b):** $d_p = 0.5$ mm at 30 dB. **(c):** $d_p = 1$ mm at 30 dB.

**Figure 3.10:** Focused views of $\Delta = \Delta(\mathbf{x})$ in the parietal region, in the case of Dipole Scan.

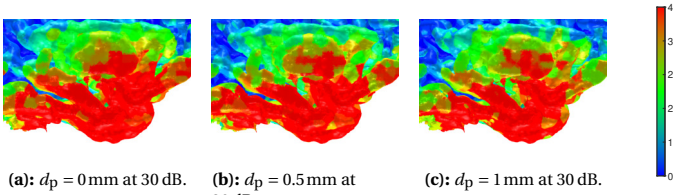


**(a):** $d_p = 0$ mm at 30 dB. **(b):** $d_p = 0.5$ mm at 30 dB. **(c):** $d_p = 1$ mm at 30 dB.

**Figure 3.11:** Focused views of $\Delta = \Delta(\mathbf{x})$ in the thalamic region, in the case of Dipole Scan.

lobe in front of the thalamus decreases, as $d_p$ is increased. A similar effect can be seen in Figure 3.8, where localisation error in the cerebrum, in front of the central sulcus decreases.

We now observe the dispersion measures of equation (2.13) for sLORETA and Dipole Scan at 30 dB noise level. These are presented in Figures 3.12 and 3.13, respectively. The ROI of dispersion around each source position was set at 30 mm.

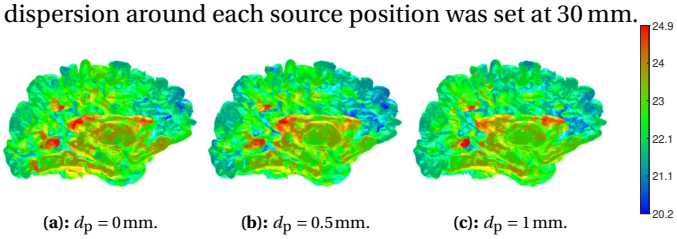


**(a):** $d_p = 0$ mm. **(b):** $d_p = 0.5$ mm. **(c):** $d_p = 1$ mm.

**Figure 3.12:** Dispersion of equation (2.13) (in mm) of sLORETA at 30 dB noise level in each position in the active gray matter layer.

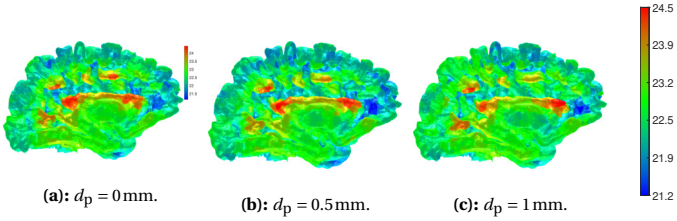


**(a):** $d_p = 0$ mm. **(b):** $d_p = 0.5$ mm. **(c):** $d_p = 1$ mm.

**Figure 3.13:** Dispersion of equation (2.13) (in mm) of Dipole Scan at 30 dB noise level in each position in the active gray matter layer.

We see a clear reduction in the width of the peak around the reconstructed dipoles, both around the thalamic region and in the cortex. For example the dipersion at the back of the thalamic region decreases from roughly 24.5 mm to 23.5 mm between Subfigures **(a)**–**(c)** of Figure 3.12. A similar effect can be observed with Dipole Scan in the subfigures of Figure 3.13.

To observe how a reduction in the number of brain layers, and more specifically the removal of the inactive white matter layer, might affect the reconstructions $\mathbf{J}_p^{\wedge}$ calculated via sLORETA and Dipole Scan, we performed reconstructions of a single tangential source with SNR = 30 dB, in the central

sulcus, with both tissue configurations seen in Figure 3.14. The removal of white matter corresponds to a change in the prior assumptions related to possible source positions, as only compartments of gray matter may contain activity, due to the presence of apical dendrites in the tissue [7][16][72].

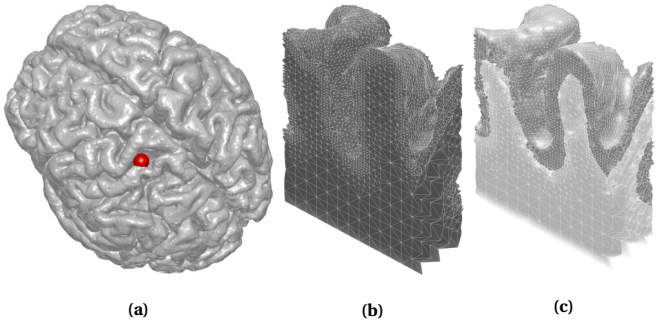


**Figure 3.14:** A structure of the mesh around the central sulcus (**a**), when (**b**), the white matter has been transformed to gray matter, and (**c**), when the inactive white matter layer is present as a separate compartment.

The reconstructions themselves are seen in Figures 3.15 and 3.16, where the first one corresponds to sLORETA and the latter shows a Dipole Scan distribution. In Figures 3.15 (**a**)–3.15 (**c**) and Figures 3.16 (**a**)–3.16 (**c**) the white matter layer has been converted to gray matter, whereas in Figures 3.15 (**d**)–3.15 (**f**) and Figures 3.16 (**d**)–3.16 (**f**) the white matter layer is present. The peeling depth $d_\mathrm{p} \in \{0.0, 0.5, 1.0\}$ mm increases from left to right.

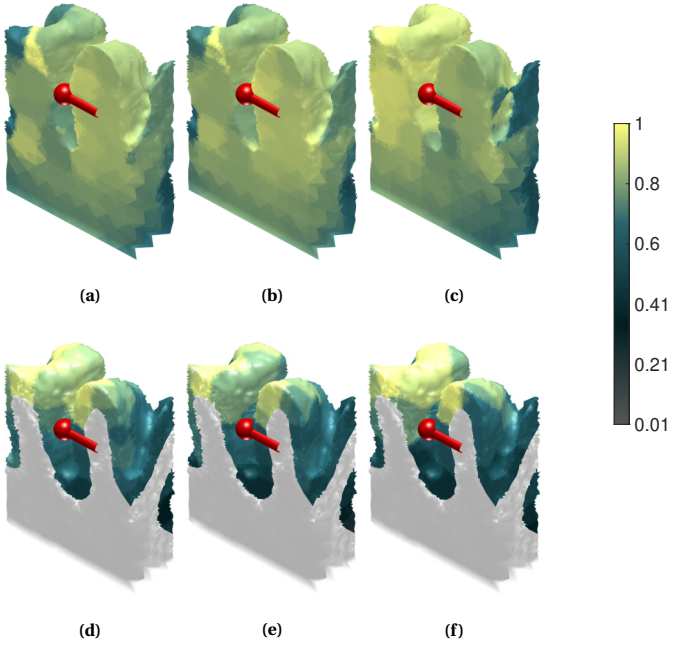


**Figure 3.15:** Relative strengths $\|\mathbf{J}_\mathrm{p}^\wedge\|$ of reconstructed primary currents $\mathbf{J}_\mathrm{p}^\wedge$, built from a positive coronal -facing dipole with SNR = 30 dB, in the central sulcus via sLORETA. Cases of $d_\mathrm{p} \in \{0.0, 0.5, 1.0\}$ mm with a removed white matter layer are shown in the respective Subfigures (**a**)–(**c**), whereas reconstructions at the same respective set of $d_\mathrm{p}$ with an included white matter is presented in Subfigures (**d**)–(**f**).

Figure 3.15 shows the patch-like nature of reconstructions

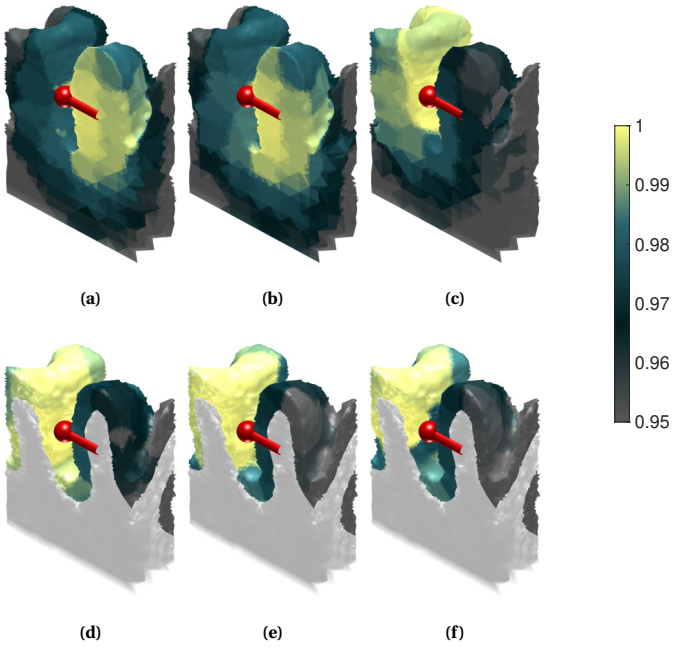


**Figure 3.16:** Relative strengths $\|\mathbf{J}_\mathrm{p}^\wedge\|$ of reconstructed primary currents $\mathbf{J}_\mathrm{p}^\wedge$, built from a positive coronal -facing dipole with SNR = 30 dB, in the central sulcus via Dipole Scan. Displays the same peeling depths $d_\mathrm{p}$ as Figure 3.15, but with $\|\mathbf{J}_\mathrm{p}^\wedge\|$ thresholded to the upper 95 % quantile, as the peak of activity produced by Dipole Scan is too wide for the differences to be visible otherwise.

generated via sLORETA. It also shows, that if the white matter layer is not present, the reconstruction $\mathbf{J}_\mathrm{p}^\wedge$ becomes less focal in the cortex, which is indicated by the extended patches of high activity on the surface of the gray matter layer. The activity also spreads further down into the now-active volume, as the lack of white matter during the construction of the forward model $\mathbf{L}$ causes it to be built, as if primary sources could be positioned there. As the forward model is biased towards the inactive white matter due to its transformation into gray matter, so is $\mathbf{J}_\mathrm{p}^\wedge$, as the utilized inverse methods rely on $\mathbf{L}$ being constructed properly. A similar effect is seen with Dipole Scan in Figure 3.16, although the restriction to the upper 95 % quantile makes this less apparent.

With sLORETA, the effect of varying the peeling depth $d_\mathrm{p}$ is better seen in the case, when white matter is present. In Figure 3.15, the already clearly active regions with $\|\mathbf{J}_\mathrm{p}^\wedge\| \geq 0.7$ become brighter, while the regions where $\|\mathbf{J}_\mathrm{p}^\wedge\|$ is fainter become more so. If the white matter has been removed, it is more difficult to pinpoint how $\mathbf{J}_\mathrm{p}^\wedge$ behaves, as peeling is added, but it seems to move slightly towards the negative direction of the dipole moment. With Dipole Scan, the case of included white matter behaves similarly to that of sLORETA, but in the case of missing white matter the peeling seems to slightly improve localisation when moving from $d_\mathrm{p} = 0$ mm to 0.5 mm. However, increasing the peeling further seems to misplace the reconstruction into the wrong gyrus in Figure 3.16 (**c**). This is again in the direction of the negative dipole moment of the original source.

## 4. Discussion

This study investigated source space peeling as a potential way to improve the forward and therefore inverse solutions of EEG source localization problem. The justification for this approach is based on increasing the distance between the source and the tissue boundaries. The relevance of this comes from the modelling errors, which can be assumed to be the greatest in the vicinity of the source [9][10][12][14][15]. Secondly, the discontinuities of the electrical conductivity at the tissue boundaries are known to decrease the regularity of the forward solution [9][13][73], enhancing any errors occurring close to a source position.

A need for introducing the present peeling technique comes from our aim to apply realistic multi-compartment head models [24], where the brain activity is limited to the thin cortical gray matter layer. For even a healthy adult subject with a relatively thick cortex, its thickness is known to be 1–4.5 mm [19]. Previous studies, such as [73], have recognized the regularizing effect of increasing the distance between the source and a tissue boundary. However, an in-depth analysis of the peeling effects, that is in the focus of this study, has not been performed previously. Notably, our approach to refine the FE mesh towards the boundaries of the thin active tissue structures allowed the creation of a solid peeling layer that is separate from the active part — an important feature to guarantee that there is no leakage of the modelled current fields through those structures, which has been documented for meshes without solid boundary layers [48].

EEG source modelling is often performed on spherical head models [4][40][74], or head models that are realistically shaped, but which only contain 3 or 4 brain compartments, such as gray matter, skull, skin and maybe the cerebrospinal fluid layers [41]. In addition, instead of these models being volumetric, only boundaries of the modelled brain compartments might be included, if forward modelling is based on boundary element methods [7][8]. Those are less resource-intensive than finite element methods, but also do not model the volumetric aspects of the problem as accurately [15][45].

FreeSurfer's [75] MRI segmentation routine, which we applied on an open dataset [66] in generating a multi-compartment finite element mesh [24], distinguishes altogether 19 different brain tissue types, excluding inhomogeneities within these major compartments, such as different types of bone in the skull [76]. Each compartment can have its own isotropic or anisotropic conductivity structure, which affects the forward solution $\mathbf{L}$. With significantly fewer compartments, modelling the subtleties of the strongly folded three-dimensional tissue structure can become difficult [33][45][74][77]. To prevent $\mathbf{L}$ from becoming biased towards regions of the brain, that cannot possibly contain activity, the set of primary dipoles $\mathbf{J}_\mathrm{p}$ was restricted to realistically shaped and volumetrically refined compartments of gray matter, where especially the cortical portion is only a few mm thick. This again required (as one option) the use of the tightly supported $H(\mathrm{div})$ source model [12], which allowed the placement of dipoles with nonzero lengths into these thin gray matter layers.

In this setting, we investigated how peeling, or the creation of source-free tetrahedral layers in the vicinity of active tissue surfaces, affects the source localisation error $\Delta$ of sLORETA [17][54] and Dipole Scan [18]. The applied *peeling depths* $d_\mathrm{p}$ were 0.0, 0.5 and 1.0 mm. The relevance of this study comes from the well-known fact, that the convergence of the forward EEG solution is negatively affected, when sources are placed near conductivity discontinuities at said tissue boundaries. This applies both to boundary element methods [78][79], and different finite element approaches, such as the Subtraction Method [9] and the $H(\mathrm{div})$ approach [13], which was used in this paper. This again negatively affects the localisation of synthetic sources via different inverse methods.

All computations were conducted using the open MATLAB package Zeffiro Interface [11][12][23][24][25][80][81][82], which allows one to perform most of the steps involved in EEG and MEG source modelling: building a finite element mesh from a surface segmentation, produced by software such as FreeSurfer [75], and constructing a lead field, in addition to a set of inverse solutions via different methods like the ones used in this work. Alternative software packages include Brainstorm [77] and DUNEuro [83]. The first of these is similar to Zeffiro Interface in capability, encompassing both forward and inverse solvers, while the latter specializes in building finite element forward solutions in electromagnetic brain imaging.

The peeling algorithm, which restricts the source positions to a distance of $d_\mathrm{p}$ from gray matter surfaces, was found to function as expected: it recognized the intended tetrahedra and always disqualified at least one layer from the surfaces of the specified brain layers, to prevent singularities from appearing in the forward solution because of discontinuities, or jumps in conductivities between neighbouring source tetra. The only anomaly related to the source positioning after peeling was that the $d_\mathrm{p} = 0.5$ mm case seemed to contain *more* sources than the $d_\mathrm{p} = 0$ mm case. This can be explained with Zeffiro Interface's iterative way of evenly distributing sources into the active volume, if the initial guess is not near the user-given amount.

Comparing the forward solution $\mathbf{L}$ to that of the semi-analytical 3-layer Ary model [4] produced appropriately good results, even at above 98 % eccentricities, where cortical sources are known to reside, but where the errors are also known to be more extensive [10]. In this case, the upper 75 % quantiles of *magnitude measure* (MAG) and *relative difference measure* (RDM) ended up being at most 0.06 and 0.04, respectively. Both of these measures being close to 0 signaled, that the forward solution was indeed well-formed. It was not obvious, whether a more refined mesh would diminish differences between the semi-analytical and numerical solutions. In fact, having a more refined mesh seems to produce deteriorated median results in the case of MAG, whereas with RDM the outcome is slightly improved. This was especially true when *Position-Based Optimization* (PBO) [63] was used for synthetic source interpolation, and hence it was chosen

as the optimization method in the case of the realistic head model. *Mean Position and Orientation* (MPO) [30] was also considered, but was deemed less suitable, as according to [13] MPO is less stable than PBO.

When looking at the average localisation errors $\Delta$, and comparing the results to those of Cuffin et. al. [71], one can observe that the performance of sLORETA is inferior to that of Dipole Scan. The reported $\Delta < 10.5\,\text{mm}$ is only reached at lower noise levels, when SNR $\geq 30\,\text{dB}$, whereas with Dipole Scan an average within acceptable boundaries can be obtained all the way down to SNR = 15 dB. In the case of sLORETA, the peeling cannot be said to improve the average localisation accuracy, as utilizing it seems to first improve the result when going from a peeling depth $d_\text{p} = 0\,\text{mm}$ to $d_\text{p} = 0.5\,\text{mm}$, but then localisation accuracy is decreased again, when $d_\text{p}$ is increased to 1 mm. Only at the very highest SNR can a slight but systematic decrease in the average $\Delta$ be seen. Dipole Scan is slightly more consistent in its performance with respect to peeling, as with SNR $\geq 20\,\text{dB}$ the added peeling no longer increases the average $\Delta$. It should be noted, that Cuffin used a 3-compartment boundary element model with a simplex search method to locate sources [84], and hence our results are not directly comparable.

The behaviour of localisation error outliers also reflect the above state of matters. In the case of sLORETA, the initial impression is that peeling seems to reduce the general denseness of the outliers clouds further above the box plots [70], but at the same time some maximum outliers are further away from the tops of the whiskers, especially in the case of $d_\text{p} = 0.5\,\text{mm}$. Peeling somewhat increases the number of outliers for the inverse method at higher SNR, although with SNR $< 20\,\text{dB}$ there seem to be cases where the outliers are reduced with added peeling. A possible explanation for this is that peeling reduces statistical variability in the low-SNR cases of sLORETA. Dipole Scan again performs more consistently, with the numbers of outliers being reduced at every SNR $\geq 15\,\text{dB}$, when the peeling depth $d_\text{p}$ is increased. It might then be said that for Dipole Scan, the effects of random noise seem to dominate when SNR is reduced beyond this point.

When observing the localisation error as a function of primary dipole position, $\Delta = \Delta(\mathbf{x})$ of sLORETA and Dipole Scan, the superior performance of the latter becomes obvious. With sLORETA, while the actual scale of the localisation error is reduced as SNR increases, we end up having more outliers with a relatively large $\Delta$ in the entire volume. In contrast, the behaviour of Dipole Scan is again more consistent: not only does the localisation error go down with increasing SNR, as one would expect, but the localisation error outliers become more focused into the deep structures of the brain, where the sources are further away from the sensors.

The benefits of increasing the peeling depth $d_\text{p}$ are also not unambiguous in either case. It seems that especially in the case of sLORETA, increasing $d_\text{p}$ simply moves the positions where outliers occur around the volume, instead of eliminating them. There are still places where the areas containing larger errors become less focal, such as in the parietal region at SNR = 25 dB. The fluctuation of the higher localisation error patches around the volume is also visible in the case of Dipole Scan, although maybe to a lesser extent. The consistent reduction in $\Delta$ with increased peeling seems to be slightly more prominent, as can be seen in the environment of *corpus callosum* and around the lower part of the frontal lobe at SNR between 20–30 dB. The takeaway from this is, that peeling the active brain layers does not guarantee unambiguously better localisation results, but that it might do so on a regional and SNR basis.

The dispersion measures of the results of different inverse methods were seen to be improved, with parts of regions of largest dispersions seeing a reduction of 1.0 mm in the width of the peak around a reconstructed dipole position. This is yet another indication of the reconstruction becoming more focal in those regions, as a reduction in dispersion indicates, that the amplitude of $\mathbf{J}_\text{p}^\wedge$ is reduced in the 30 mm ROI for the dispersion around each respective source position, with the most focal point being at the center of the ROI.

Finally, we presented examples of how replacing the inactive white matter layer with gray matter might affect the inverse solution, in a case where activity was generated by a single tangential dipole in the cortex. The replacement had the main effect of biasing the reconstructed activity $\mathbf{J}_\text{p}^\wedge$ towards the white matter layer, which should not contain primary activity $\mathbf{J}_\text{p}$ in the first place [7][16]. This biasing is simply the result of the forward solution being constructed, as if the white matter layer could contain activity. Since the inverse solvers depend on the forward solution encoding correct prior information, which is not the case when white matter has been removed, we end up with reconstructions in incorrect positions. Our results are in accordance with other discussions on the significance of white vs. gray matter distinction [41][45][85]. The effects of varying the peeling depth $d_\text{p}$ seemed to manifest themselves as the transition of the peak of $\mathbf{J}_\text{p}^\wedge$ towards the negative dipole moment of the source. Too much peeling had the potential of misplacing the peak of activity into an entirely wrong cortixcal gyrus, in the mentioned direction. The peaks of $\mathbf{J}_\text{p}^\wedge$ also became less wide, which was especially visible when the white matter layer was present.

## 5. Conclusions

*Summa summarum*, while restricting the synthetic dipoles $\mathbf{J}_\text{p}$, that model brain activity to be further away from active brain compartment boundaries, and therefore from conductivity jumps, the reconstructed distribution of dipoles $\mathbf{J}_\text{p}^\wedge$ is altered, but not definitely improved. The peeling algorithm responsible for the application of the above restriction was enabled by a local refinement or resolution increase of the finite element mesh, and was shown to uniformly reduce statistical outliers in the forward solution $\mathbf{L}$, which maps $\mathbf{J}_\text{p}$ to the observed potentials at the EEG electrodes, thereby increasing its robustness.

This reduction in outliers is best observed with noise levels below 30 dB, which occur in medical studies, where possibly thousands of stimuli might be applied over the duration

of the experiment, such as when measuring somatosensory-evoked potential responses [86]. In addition to improving the robustness of the forward solution, peeling had the same effect on the reconstruction, in addition to enhancing the regularity of it. The importance of the regularity of a reconstruction comes from the need to locate multiple or distributed sources, such as in the case of localising epileptogenic zones or their irritative regions for the purposes of treatment [87][88].

## 6. Future prospects

Follow-up studies might include further increasing the base resolution and/or the refinement of the active layers in the mesh, so that the possible locations of dipoles would become more varied. Peeling depths might also be observed in a wider or more refined range than was presented in this study, to find out whether there is some optimal value for it. This optimal value might depend on the mesh geometry, and therefore the tests might be performed on multiple different head models with the same mesh resolution.

For case studies, the use of the peeling technique might be applied to head models of patients with conditions such as *microlissencephaly* [89], where the cortex is flattened and possibly thickened. A *schizencephalic* [89][90] brain model, where a part of the brain has been displaced, and the displaced sections are connected only by a thin ribbon of gray matter is another possibly interesting target of peeling.


## Acknowledgements

This work has been supported by **(1)** the Academy of Finland (AoF) Centre of Excellence (CoE) in Inverse Modelling and Imaging 2018-2025, **(2)** by the AoF project #344712 and the Bundesministerium für Gesundheit (BMG) project ZMI1-2521FSB006, under the frame of ERA PerMed as project ERAPERMED2020-227 (PerEpi), **(3)** by the bilateral AoF and DAAD projects #354976 and #57663920, and **(4)** by Vilho, Yrjö and Kalle Väisälä Fund (VYKVF). Per author, the funding sources were as follows: Santtu Söderholm (AoF/PerEpi), Joonas Lahtinen (VYKVF), Carsten H. Wolters (DAAD/PerEpi) and Sampsa Pursiainen (CoE, AoF/PerEpi).


## Declaration of competing interests

The authors declare that they have no known competing financial interests or personal relationships, that could have appeared to influence the work reported in this paper.

## Appendix A. Use of Zeffiro Interface in this study

In this appendix, we present the settings or input values used in constructing the different data structures needed in this study. These include the finite element mesh, forward solution or lead field **L**, and the inverse reconstructions. The settings are stored in the central data structure `zef`, by assigning them to it with the syntax `zef.field_name=field_value;`, after starting up Zeffiro Interface on the MATLAB command line with `zef=zeffiro_interface;`. The version of Zeffiro Interface used was `2bcd38f3` [26]. Also, throughout the below listings, the symbol `|` is used to denote alternative values of variables.

### *Appendix A.1. Finite element mesh generation*

```
zef.adaptive_refinement_compartments = 1 ;
zef.adaptive_refinement_k_param = 10 ;
zef.adaptive_refinement_number = 1 ;
zef.adaptive_refinement_on = false ;
zef.adaptive_refinement_thresh_val = 0.9 ;
zef.exclude_box = true ;
zef.fem_mesh_inflation_strength = 0.3 ;
zef.fix_outer_surface = true ;
zef.initial_mesh_mode = 1 ;
zef.mesh_labeling_approach = 1 ;
zef.mesh_optimization_parameter = 1e-5 ;
zef.mesh_optimization_repetitions = 30 ;
zef.mesh_relabeling = true ;
zef.mesh_resolution = 2 ;
zef.mesh_smoothing_on = true ;
zef.mesh_smoothing_repetitions = 1 ;
zef.meshing_threshold = 0.25 ;
zef.pml_max_size = 2 ;
zef.pml_max_size_unit = 1 ;
zef.pml_outer_radius = 1.05 ;
zef.pml_outer_radius_unit = 1 ;
zef.reduce_labeling_outliers = true ;
zef.refinement_on = true ;
zef.refinement_surface_compartments = ...
        [19, 18, 1, 13, 11] ;
zef.refinement_surface_compartments_2 = ...
        [19, 18, 1, 13, 11] ;
zef.refinement_surface_number = 2 ;
zef.refinement_surface_number_2 = 1 ;
zef.refinement_surface_on = true ;
zef.refinement_surface_on_2 = false ;
zef.refinement_volume_compartments = [ 1 , 19 , 18 ] ;
zef.refinement_volume_compartments_2 = [ 1, 16, 12 ] ;
zef.refinement_volume_number = 1 ;
zef.refinement_volume_number_2 = 1 ;
zef.refinement_volume_on = false ;
zef.refinement_volume_on_2 = true ;
zef.smoothing_steps_ele = 0.2 ;
zef.smoothing_steps_surf = 0.10 ;
zef.smoothing_steps_vol = 0.90 ;
zef.use_fem_mesh_inflation = true ;
zef = zef_create_finite_element_mesh ( zef ) ;
```

### *Appendix A.2. Lead field generation*

```
zef.acceptable_source_depth = 0|0.5|1 ; % Peeling depth
zef.lead_field_filter_quantile = 1 ;
zef.lead_field_type = 1 ;
zef.lf_normalization = 1 ;
zef.location_unit = 1 ;
zef.n_sources = 1e4 ;
zef.optimization_system_type = "pbo" ;
zef.preconditioner = 2 ;
zef.preconditioner_tolerance = 0.001 ;
zef.solver_tolerance = 1e-6 ;
zef.source_direction_mode = 1 ;
zef.source_interpolation_on = true ;
zef.source_model = core.ZefSourceModel.Hdiv ;
zef.source_space_creation_iterations = 2 ;
zef.use_depth_electrodes = false ;
zef = zef_eeg_lead_field ( zef ) ;
```

*Appendix A.3. Constructing the localisation error results*

To start off, one should construct a finite element mesh and a set of lead fields, using the settings in Appendix A.1 and Appendix A.2, and then save the results corresponding to different peeling depths to their own Zeffiro Interface project files. With the mesh and lead fields in place, one may start the reconstructions by calling the function `examples.studies.santtus_peeling_article.main`, which allows adjusting the relevant settings via its arguments:

```
[stats, L] ...
= ...
examples.studies.santtus_peeling_article.main ( ...
        "path/to/project/file.mat", ...
        "sLORETA" | "Dipole Scan" , ...
        20 , ... Number of reconstructions
        -20|-25|-30 , ... Noise level
        "L2" , ... Measure of distance
        30, ... Dispersion_radius
        use_gpu = true|false , ...
        build_mesh = false , ...
        build_lead_field = false ...
) ;
```

The output struct `stats` contains the statistics related to the localisation error $\Delta$ and spatial dispersion SD seen in this study.

*Appendix A.4. Single source reconstructions*

To generate the results of Figures 3.14–3.16, we first generated another head model with the white matter layer replaced entirely with gray matter, and precomputed 6 different lead fields: one for each peeling depth $d_p \in \{0.0, 0.5, 1.0\}$ mm, both when white matter was present and when it was not. Then the single source was positioned with the Zeffiro Interface tool *Find synthetic source legacy*, at $\mathbf{x} = [-20, -40, 85]$ with the orientation $\mathbf{d} = [0, 1, 0]$. With the single source in place, we computed the reconstructions with the inverse plugins *MNE tool* and *Dipole Scan*, with sLORETA standardization and tSVD filtering, respectively.

## References


[1] H. Berger, Über das Elektrenkephalogramm des Menschen , Archiv für Psychiatrie und Nervenkrankheiten 87 (1929) 527–570. doi:10.1007/BF01797193.

[2] R. Brette, A. Destexhe (Eds.), Handbook of Neural Activity Measurement, Cambridge University Press, 2012. doi:10.1017/CBO9780511979958.

[3] J. Sarvas, Basic mathematical and electromagnetic concepts of the biomagnetic inverse problem, Physics in Medicine & Biology 32 (1) (1987) 11. doi:10.1088/0031-9155/32/1/004.

[4] J. P. Ary, S. A. Klein, D. H. Fender, Location of Sources of Evoked Scalp Potentials: Corrections for Skull and Scalp Thicknesses, IEEE Transactions on Biomedical Engineering BME-28 (6) (1981) 447–452. doi:10.1109/TBME.1981.324817.

[5] J. de Munck, M. Peters, A fast method to compute the potential in the multisphere model (EEG application), IEEE Transactions on Biomedical Engineering 40 (11) (1993) 1166–1174. doi:10.1109/10.245635.

[6] H. Hallez, B. Vanrumste, P. V. Hese, S. Delputte, I. Lemahieu, Dipole estimation errors due to differences in modeling anisotropic conductivities in realistic head models for EEG source analysis, Physics in Medicine & Biology 53 (7) (2008). doi:10.1088/0031-9155/53/7/005.

[7] M. Hämäläinen, R. Hari, R. J. Ilmoniemi, J. Knuutila, O. V. Lounasmaa, Magnetoencephalography — theory, instrumentation and applications to non-invasive studies of the working human brain, Review of Modern Physics 65 (2) (1993).

[8] J. Kybic, M. Clerc, T. Abboud, O. Faugeras, R. Keriven, T. Papadopoulo, A common formalism for the Integral formulations of the forward EEG problem, IEEE Transactions on Medical Imaging 24 (1) (2005) 12–28. doi:10.1109/TMI.2004.837363.

[9] C. H. Wolters, H. Köstler, C. Möller, J. Härdtlein, L. Grasedyck, W. Hackbusch, Numerical Mathematics of the Subtraction Method for the Modeling of a Current Dipole in EEG Source Reconstruction Using Finite Element Head Models, SIAM Journal on Scientific Computing 30 (1) (2008) 24–45. doi:10.1137/060659053.

[10] F. Drechsler, C. Wolters, T. Dierkes, H. Si, L. Grasedyck, A full subtraction approach for finite element method based source analysis using constrained Delaunay tetrahedralisation, NeuroImage 46 (4) (2009) 1055–1065. doi:10.1016/j.neuroimage.2009.02.024.

[11] Q. He, A. Rezaei, S. Pursiainen, Zeffiro User Interface for Electromagnetic Brain Imaging: a GPU Accelerated FEM Tool for Forward and Inverse Computations in Matlab, Neuroinformatics 18 (2020) 237–250. doi:10.1007/s12021-019-09436-9.

[12] T. Miinalainen, A. Rezaei, D. Us, A. Nüßing, C. Engwer, C. H. Wolters, S. Pursiainen, A realistic, accurate and fast source modeling approach for the EEG forward problem, NeuroImage 184 (2019) 56–67. doi:10.1016/j.neuroimage.2018.08.054.

[13] S. Pursiainen, J. Vorwerk, C. Wolters, Electroencephalography (EEG) forward modeling via H(div) finite element sources with focal interpolation, Physics in Medicine & Biology 61 (24) (2016).

[14] L. Beltrachini, The analytical subtraction approach for solving the forward problem in EEG, Journal of Neural Engineering 16 (5) (2019) 056029. doi:10.1088/1741-2552/ab2694.

[15] T. Knösche, J. Haueisen, EEG/MEG Source Reconstruction, Springer, 2022.

[16] S. Murakami, Y. Okada, Invariance in current dipole moment density across brain structures and species: Physiological constraint for neuroimaging, NeuroImage 111 (2015) 49–58. doi:10.1016/j.neuroimage.2015.02.003.

[17] R. D. Pascual-Marqui, Standardized low-resolution brain electromagnetic tomography (sLORETA): technical details, Methods and findings in experimental and clinical pharmacology (24) (2002) 5–12.

[18] F. Neugebauer, M. Antonakakis, K. Unnwongse, Y. Parpaley, J. Wellmer, S. Rampp, C. H. Wolters, Validating EEG, MEG and combined MEG and EEG beamforming for an estimation of the epileptogenic zone in focal cortical dysplasia, Brain Sciences 12 (1) (2022). doi:10.3390/brainsci12010114.

[19] B. Fischl, A. M. Dale, Measuring the thickness of the human cerebral cortex from magnetic resonance images, Proceedings of the National Academy of Sciences 97 (20) (2000) 11050–11055. doi:10.1073/pnas.200033797.

[20] S. Saha, Y. I. Nesterets, M. Tahtali, T. E. Gureyev, Evaluation of spatial resolution and noise sensitivity of sLORETA method for EEG source localization using low-density headsets, Biomedical Physics & Engineering Express 1 (4) (2015) 045206. doi:10.1088/2057-1976/1/4/045206.

[21] M. Carboni, D. Brunet, M. Seeber, C. M. Michel, S. Vulliemoz, B. J. Vorderwülbecke, Linear distributed inverse solutions for interictal EEG source localisation, Clinical Neurophysiology 133 (2022) 58–67. doi:10.1016/j.clinph.2021.10.008.

[22] M. Fuchs, M. Wagner, H.-A. Wischmann, T. Köhler, A. Theißen, R. Drenckhahn, H. Buchner, Improving source reconstructions by combining bioelectric and biomagnetic data, Electroencephalography and Clinical Neurophysiology 107 (2) (1998) 93–111. doi:10.1016/S0013-4694(98)00046-7.

[23] S. Pursiainen, Raviart–Thomas-type sources adapted to applied EEG and MEG: implementation and results, Inverse Problems 28 (6) (2012) 065013. doi:10.1088/0266-5611/28/6/065013.

[24] F. Galaz Prieto, J. Lahtinen, M. Samavaki, S. Pursiainen, Multi-compartment head modeling in EEG: Unstructured boundary-fitted tetra meshing with subcortical structures, PLOS ONE 18 (9) (2023) 1–25. doi:10.1371/journal.pone.0290715.

[25] F. Galaz Prieto, A. Rezaei, M. Samavaki, S. Pursiainen, L1-norm vs. L2-norm fitting in optimizing focal multi-channel tES stimulation: linear and semidefinite programming vs. weighted least squares, Computer Methods and Programs in Biomedicine 226 (2022) 107084. doi:10.1016/j.cmpb.2022.107084.

[26] S. Pursiainen, J. Lahtinen, F. Galaz Prieto, P. Ronni, F. Neugebauer, S. Söderholm, A. Rezaei, A. Lassila, A. Frank, O. Kolawole, M. Shavliuk, M. Hoeltershinken, M. Samavaki, Y. Yusuf Oluwatoki, T. Farenc, sampsapursiainen/zeffiro_interface: October2023 (Oct. 2023). doi:10.5281/zenodo.8431180.

[27] O. Hauk, M. Stenroos, M. S. Treder, Towards an objective evaluation of EEG/MEG source estimation methods – The linear approach, NeuroImage 255 (2022) 119177. doi:10.1016/j.neuroimage.2022.119177.

[28] R. De Peralta-Menendez, S. Gonzalez-Andino, A critical analysis of linear inverse solutions to the neuroelectromagnetic inverse problem, IEEE Transactions on Biomedical Engineering 45 (4) (1998) 440–448. doi:10.1109/10.664200.

[29] J. Scales, R. Snieder, The Anatomy of Inverse Problems, Geophysics 65 (09 2001). doi:10.1190/geo2000-0001.1.

[30] A. Rezaei, Forward and Inverse Modeling via Finite Elements in EEG/MEG Source Localization, Ph.D. thesis (2021).

[31] Y. Wang, J. Gotman, The influence of electrode location errors on EEG dipole source localization with a realistic head model, Clinical Neurophysiology 112 (9) (2001) 1777–1780. doi:10.1016/S1388-2457(01)00594-6.

[32] B. Lanfer, M. Scherg, M. Dannhauer, T. Knösche, M. Burger, C. Wolters, Influences of skull segmentation inaccuracies on EEG source analysis, NeuroImage 62 (1) (2012) 418–431. doi:10.1016/j.neuroimage.2012.05.006.

[33] Z. Akalin Acar, S. Makeig, Effects of forward model errors on EEG source localization, Brain topography 26 (3) (2013) 378–396.

[34] C. Phillips, M. D. Rugg, K. J. Friston, Systematic Regularization of Linear Inverse Solutions of the EEG Source Localization Problem, NeuroImage 17 (1) (2002) 287–301. doi:10.1006/nimg.2002.1175.

[35] M. Teplan, Fundamentals of EEG measurement, Measurement Science Review 2 (2) (2002) 1–11.

[36] R. Hari, A. Puce, MEG-EEG Primer, Oxford University Press, 2017. doi:10.1093/med/9780190497774.001.0001.

[37] S. Baillet, L. Garnero, A Bayesian approach to introducing anatomo-functional priors in the EEG/MEG inverse problem, IEEE Transactions on Biomedical Engineering 44 (5) (1997) 374–385. doi:10.1109/10.568913.

[38] J. Scales, L. Tenorio, Prior Information and Uncertainty in Inverse Problems, Geophysics 66 (05 2001). doi:10.1190/1.1444930.

[39] D. Calvetti, H. Hakula, S. Pursiainen, E. Somersalo, Conditionally Gaussian Hypermodels for Cerebral Source Localization, SIAM Journal on Imaging Sciences 2 (3) (2009) 879–909. arXiv:10.1137/080723995, doi:10.1137/080723995.

[40] B. J. Roth, M. Balish, A. Gorbach, S. Sato, How well does a three-sphere model predict positions of dipoles in a realistically shaped head?, Electroencephalography and Clinical Neurophysiology 87 (4) (1993) 175–184. doi:10.1016/0013-4694(93)90017-P.

[41] J. Vorwerk, J.-H. Cho, S. Rampp, H. Hamer, T. R. Knösche, C. H. Wolters, A guideline for head volume conductor modeling in EEG and MEG, NeuroImage 100 (2014) 590–607. doi:10.1016/j.neuroimage.2014.06.040.

[42] C. Ramon, P. H. Schimpf, J. Haueisen, Influence of head models on EEG simulations and inverse source localizations, Biomedical engineering online 5 (10) (2006). doi:10.1186/1475-925X-5-10.

[43] K. Wendel, N. G. Narra, M. Hannula, P. Kauppinen, J. Malmivuo, The Influence of CSF on EEG Sensitivity Distributions of Multilayered Head Models, IEEE Transactions on Biomedical Engineering 55 (4) (2008) 1454–1456. doi:10.1109/TBME.2007.912427.

[44] M. C. Piastra, A. Nüßing, J. Vorwerk, M. Clerc, C. Engwer, C. H. Wolters, A comprehensive study on electroencephalography and magnetoencephalography sensitivity to cortical and subcortical sources, Human Brain Mapping 42 (4) (2021) 978–992. doi:10.1002/hbm.25272.

[45] J.-H. Cho, J. Vorwerk, C. H. Wolters, T. R. Knösche, Influence of the head model on EEG and MEG source connectivity analyses, NeuroImage 110 (2015) 60–77. doi:10.1016/j.neuroimage.2015.01.043.

[46] G. Dassios, A. S. Fokas, D. Hadjiloizi, On the complementarity of electroencephalography and magnetoencephalography, Inverse Problems 23 (6) (2007) 2541. doi:10.1088/0266-5611/23/6/016.

[47] F. Zhang, The Schur complement and its applications, Springer, 2005. doi:10.1007/b105056.

[48] J. Vorwerk, C. Engwer, S. Pursiainen, C. H. Wolters, A Mixed Finite Element Method to Solve the EEG Forward Problem, IEEE Transactions on Medical Imaging 36 (4) (2017) 930–941. doi:10.1109/TMI.2016.2624634.

[49] M. Benning, M. Burger, Modern regularization methods for inverse problems, Acta Numerica 27 (2018) 1–111. doi:10.1017/S0962492918000016.

[50] C. Clason, Regularization of Inverse Problems, 10.48550/arXiv.2001.00617, accessed: 2022-12-14 (2021).

[51] J. Kaipio, E. Somersalo, Statistical and Computational Inverse Problems, Springer, 2004.

[52] A. J. Leal, A. I. Dias, J. P. Vieira, A. Moreira, L. Távora, E. Calado, Analysis of the dynamics and origin of epileptic activity in patients with tuberous sclerosis evaluated for surgery of epilepsy, Clinical Neurophysiology 119 (4) (2008) 853–861. doi:10.1016/j.clinph.2007.11.176.

[53] B. Van Veen, W. Van Drongelen, M. Yuchtman, A. Suzuki, Localization of brain electrical activity via linearly constrained minimum variance spatial filtering, IEEE Transactions on Biomedical Engineering 44 (9) (1997) 867–880. doi:10.1109/10.623056.

[54] K. Sekihara, S. S. Nagarajan, Adaptive Spatial Filters for Electromagnetic Brain Imaging, Springer, 2008.

[55] K. Sekihara, M. Sahani, S. Nagarajan, Localization bias and spatial resolution of adaptive and non-adaptive spatial filters for MEG source reconstruction, Neuroimage 25 (2005) 1056–1067. doi:10.1016/j.neuroimage.2004.11.051.

[56] R. Greenblatt, A. Ossadtchi, M. Pflieger, Local linear estimators for the bioelectromagnetic inverse problem, IEEE Transactions on Signal Processing 53 (9) (2005) 3403–3412. doi:10.1109/TSP.2005.853201.

[57] A. Rezaei, M. Antonakakis, M. Piastra, C. H. Wolters, S. Pursiainen, Parametrizing the Conditionally Gaussian Prior Model for Source Localization with Reference to the P20/N20 Component of Median Nerve SEP/SEF, Brain Sciences 10 (12) (2020). doi:10.3390/brainsci10120934.

[58] C. Wolters, R. Beckmann, A. Rienäcker, H. Buchner, Comparing Regularized and Non-Regularized Nonlinear Dipole Fit Methods: A Study in a Simulated Sulcus Structure, Brain Topography 12 (1999) 3–18. doi:10.1023/A:1022281005608.

[59] D. Braess, Finite Elements, Cambridge University Press, 2007.

[60] D. Weinstein, L. Zhukov, C. Johnson, Lead-field Bases for Electroencephalography Source Imaging, Annals of Biomedical Engineering 28 (2000) 1059–1065. doi:10.1114/1.1310220.

[61] M. B. Höltershinken, Efficient Computation of Transfer Matrices using the Block Conjugate Gradient Method, Master's thesis, University of Münster (2021).

[62] E. Ziegler, S. L. Chellappa, G. Gaggioni, J. Q. Ly, G. Vandewalle, E. André, C. Geuzaine, C. Phillips, A finite-element reciprocity solution for EEG forward modeling with realistic individual head models, NeuroImage 103 (2014) 542–551. doi:10.1016/j.neuroimage.2014.08.056.

[63] M. Bauer, S. Pursiainen, J. Vorwerk, H. Köstler, C. H. Wolters, Comparison Study for Whitney (Raviart–Thomas)-Type Source Models in Finite-Element-Method-Based EEG Forward Modeling, IEEE Transactions on Biomedical Engineering 62 (11) (2015) 2648–2656. doi:10.1109/TBME.2015.2439282.

[64] C. H. Wolters, A. Anwander, G. Berti, U. Hartmann, Geometry-Adapted Hexahedral Meshes Improve Accuracy of Finite-Element-Method-Based EEG Source Analysis, IEEE Transactions on Biomedical Engineering 54 (8) (2007) 1446–1453. doi:10.1109/TBME.2007.890736.

[65] D. Güllmar, J. Haueisen, J. R. Reichenbach, Influence of anisotropic electrical conductivity in white matter tissue on the EEG/MEG forward and inverse solution. A high-resolution whole head simulation study, NeuroImage 51 (1) (2010) 145–163. doi:10.1016/j.neuroimage.2010.02.014.

[66] M. C. Piastra, S. Schrader, A. Nüßing, M. Antonakakis, T. Medani, A. Wollbrink, C. Engwer, C. H. Wolters, The WWU DUNEuro reference data set for combined EEG/MEG source analysis, The research related to this dataset was supported by the German Research Foundation (DFG) through project WO1425/7-1 and the EU project ChildBrain (Marie Curie Innovative Training Networks, grant agreement 641652). (jun 2020). doi:10.5281/zenodo.3888381.

[67] M. Hämäläinen, R. Ilmoniemi, Interpreting magnetic fields of the brain: minimum-norm estimates. Med Biol Eng Comput 32: 35-42, Medical & biological engineering & computing 32 (1994) 35–42. doi:10.1007/BF02512476.

[68] I. S. Mohamed, H. Otsubo, P. Ferrari, R. Sharma, A. Ochi, I. Elliott, C. Go, S. Chuang, J. Rutka, C. Snead, D. Cheyne, Source localization of interictal spike-locked neuromagnetic oscillations in pediatric neocortical epilepsy, Clinical Neurophysiology 124 (8) (2013) 1517–1527. doi:10.1016/j.clinph.2013.01.023.

[69] A. Molins, S. Stufflebeam, E. Brown, M. Hämäläinen, Quantification of the benefit from integrating MEG and EEG data in minimum l2-norm estimation, NeuroImage 42 (3) (2008) 1069–1077. doi:10.1016/j.neuroimage.2008.05.064.

[70] R. Mcgill, J. W. Tukey, W. A. Larsen, Variations of Box Plots, The American Statistician 32 (1) (1978) 12–16. doi:10.1080/00031305.1978.10479236.

[71] B. Cuffin, D. L. Schomer, J. R. Ives, H. Blume, Experimental tests of EEG source localization accuracy in realistically shaped head models, Clinical Neurophysiology 112 (12) (2001) 2288–2292. doi:10.1016/S1388-2457(01)00669-1.

[72] M. Rullmann, A. Anwander, M. Dannhauer, S. Warfield, F. Duffy, C. Wolters, EEG source analysis of epileptiform activity using a 1 mm anisotropic hexahedra finite element head model, NeuroImage 44 (2) (2009) 399–410. doi:10.1016/j.neuroimage.2008.09.009.

[73] J. Vorwerk, U. Aydin, C. H. Wolters, C. R. Butson, Influence of Head Tissue Conductivity Uncertainties on EEG Dipole Reconstruction, Frontiers in Neuroscience 13 (2019). doi:10.3389/fnins.2019.00531.

[74] F. Meneghini, F. Esposito, S. Mininel, F. Di Salle, F. Vatta, F. Babiloni, Realistic and Spherical Head Modeling for EEG Forward Problem Solution: A Comparative Cortex-Based Analysis, Computational Intelligence and Neuroscience 2010 (2010). doi:10.1155/2010/972060.

[75] B. Fischl, FreeSurfer, NeuroImage 62 (2) (2012) 774–781, 20 YEARS OF fMRI. doi:10.1016/j.neuroimage.2012.01.021.

[76] M. Dannhauer, B. Lanfer, C. H. Wolters, T. R. Knösche, Modeling of the human skull in EEG source analysis, Human Brain Mapping 32 (9) (2011) 1383–1399. doi:10.1002/hbm.21114.

[77] F. Tadel, E. Bock, G. Niso, J. C. Mosher, M. Cousineau, D. Pantazis, R. M. Leahy, S. Baillet, MEG/EEG Group Analysis With Brainstorm, Frontiers in Neuroscience 13 (2019). doi:10.3389/fnins.2019.00076.

[78] B. He, Y. Wang, D. Wu, Estimating cortical potentials from scalp EEGs in a realistically shaped inhomogeneous head model by means of the boundary element method, IEEE Transactions on Biomedical Engineering 46 (10) (1999) 1264–1268. doi:10.1109/10.790505.

[79] M. Fuchs, M. Wagner, J. Kastner, Boundary element method volume conductor models for EEG source reconstruction, Clinical Neurophysiology 112 (8) (2001) 1400–1407. doi:10.1016/S1388-2457(01)00589-2.

[80] A. Rezaei, A. Koulouri, S. Pursiainen, Randomized Multiresolution Scanning in Focal and Fast E/MEG Sensing of Brain Activity with a Variable Depth, Brain Topography 33 (2020) 161–175. doi:10.1007/s10548-020-00755-8.

[81] J. Lahtinen, F. Moura, M. Samavaki, S. Siltanen, S. Pursiainen, In silico study of the effects of cerebral circulation on source localization using a dynamical anatomical atlas of the human head, Journal of Neural Engineering 20 (2) (2023) 026005. doi:10.1088/1741-2552/acbdc1.

[82] M. Samavaki, Y. Oluwatoki Yusuf, A. Z. Nia, S. Söderholm, J. Lahtinen, F. Galaz Prieto, S. Pursiainen, Pressure–Poisson Equation in Numerical Simulation of Cerebral Arterial Circulation and Its Effect on the Electrical Conductivity of the Brain, Computer Methods and Programs in Biomedicine (107844) (2023). doi:10.1016/j.cmpb.2023.107844.

[83] S. Schrader, A. Westhoff, M. C. Piastra, T. Miinalainen, S. Pursiainen, J. Vorwerk, H. Brinck, C. H. Wolters, C. Engwer, DUNEuro—A software toolbox for forward modeling in bioelectromagnetism, PLOS ONE 16 (6) (2021) 1–21. doi:10.1371/journal.pone.0252431.

[84] W. H. Press, S. A. Teukolsky, W. T. Vetterling, B. P. Flannery, Numerical recipes 3rd edition: The art of scientific computing, Cambridge university press, 1989.

[85] C. Ramon, P. Schimpf, J. Haueisen, M. Holmes, A. Ishimaru, Role of Soft Bone, CSF and Gray Matter in EEG Simulations, Brain Topography 16 (2004) 245–248. doi:10.1023/B:BRAT.0000032859.68959.76.

[86] G. Cruccu, M. Aminoff, G. Curio, J. Guerit, R. Kakigi, F. Mauguiere, P. Rossini, R.-D. Treede, L. Garcia-Larrea, Recommendations for the clinical use of somatosensory-evoked potentials, Clinical Neurophysiology 119 (8) (2008) 1705–1719. doi:10.1016/j.clinph.2008.03.016.

[87] P. van Mierlo, B. J. Vorderwülbecke, W. Staljanssens, M. Seeck, S. Vulliémoz, Ictal EEG source localization in focal epilepsy: Review and future perspectives, Clinical Neurophysiology 131 (11) (2020) 2600–2616. doi:10.1016/j.clinph.2020.08.001.

[88] M. Fernandez-Corazza, R. Feng, C. Ma, J. Hu, L. Pan, P. Luu, D. Tucker, Source localization of epileptic spikes using Multiple Sparse Priors, Clinical Neurophysiology 132 (2) (2021) 586–597. doi:10.1016/j.clinph.2020.10.030.

[89] A. A. Razek, A. Kandell, L. Elsorogy, A. Elmongy, A. Basett, Disorders of Cortical Formation: MR Imaging Features, American Journal of Neuroradiology 30 (1) (2009) 4–11. doi:10.3174/ajnr.A1223.

[90] J. LoTurco, A. Booker, Chapter 26 - Neuronal Migration Disorders, in: J. L. Rubenstein, P. Rakic (Eds.), Cellular Migration and Formation of Neuronal Connections, Academic Press, Oxford, 2013, pp. 481–494. doi:10.1016/B978-0-12-397266-8.00038-7.